Experimental and numerical investigation of the transition from non sooting to sooting premixed n-butane flames, encompassing the nucleation flame conditions

Christopher Betrancourt, Damien Aubagnac-Karkar, Xavier Mercier, Abderrahman El-Bakali, Pascale Desgroux

Experimental and numerical investigation of the transition from non sooting to sooting premixed n-butane flames, encompassing the nucleation flame conditions.

Christopher Betrancourt[1,*], Damien Aubagnac-Karkar[2], Xavier Mercier[3], Abderrahman El-Bakali[3], Pascale Desgroux[3,*]

[1] *Laboratoire EM2C, CNRS, CentraleSupélec, Université Paris-Saclay, 3 rue Joliot Curie, Gif-sur-Yvette cedex 91192, France*

[2] *IFP Energies nouvelles, 1 et 4 avenue de Bois-Préau, 92852 Rueil-Malmaison, France*

[3] *Univ. Lille, CNRS, UMR 8522 - PC2A - Physicochimie des Processus de Combustion et de l'Atmosphère, F-59000 Lille, France*

*** Corresponding authors**:

Pascale Desgroux

Univ. Lille, CNRS, UMR 8522 - PC2A - Physicochimie des Processus de Combustion et de l'Atmosphère, F-59000 Lille, France.

E-mail: pascale.desgroux@univ-lille.fr

Christopher Betrancourt

Laboratoire EM2C, CNRS, CentraleSupélec, Université Paris-Saclay, 3, rue Joliot Curie, Gif-sur-Yvette cedex 91192, France

E-mail: christopher.betrancourt@centralesupelec.fr

Full-Length Article

Color figures in electronic version only

7 Supplemental Materials are available

Abstract

In a small range of rich equivalence ratios, premixed flat flames, so-called nucleation flames, were shown to produce very small-size (2-4 nm) soot particles, which undergo negligible growth with the residence time. In such flames, the contribution of the soot nucleation step with respect to the soot growth process is larger than in standard sooting flames, making nucleation flames ideal target flames to better understand the inception process. In order to scrutinize the transition from non sooting to sooting flames, three premixed atmospheric n-butane/oxygen/nitrogen flames surrounding the nucleation flame conditions were investigated: the flame at ϕ=1.6 is a fuel-rich non-sooting flame, the flame at ϕ=1.75 is a nucleation flame and the flame at ϕ=1.95 is a lightly sooting flame. The soot volume faction (SVF) profiles were previously measured by laser-induced incandescence as well as the soot size distributions. In the present study, mole fractions of stable species up to benzene were measured by gas chromatography while those of naphthalene and pyrene were obtained by jet-cooled laser-induced fluorescence. It is found that acetylene, propyne, benzene, naphthalene and pyrene species show the highest sensitivity with the equivalence ratio, while a two orders of magnitude increase of SVF is observed. The chemical flame structure of these flames was modeled using three kinetic mechanisms of the literature to which a recently developed soot code, based on a sectional approach, was coupled. The chosen model is representative of the current state-of-the-art of models describing all steps of soot formation and growth and fully coupled with the gas phase. The ability of such a model to predict soot volume fraction with reasonable predictions of gas-phase species is validated here based on the new experimental database presented in this work. It also highlights the improvement required on particle inception modeling to correctly predict particle size distributions.

Keywords: butane, flame, soot, modelling, PAH

1 Introduction

Reducing soot emission from combustion-based energy systems is a major concern because of the negative effect of soot particles on health, environment and climate. Soot abatement is closely linked to the control of soot formation process in flames. However, the complete description of the soot formation process is confronted to the stumbling block linked to the understanding of the soot nucleation step i.e. the transition from the gas phase to the soot particles. Many studies focused on this topic but both the process itself and the gaseous species involved are still not clearly understood. Polycyclic aromatic hydrocarbons (PAHs) have been known to be closely related to soot nucleation [1,2]. Recent studies show that more complex species created by combination of small to moderate PAHs [3–5] and potentially involving dimerization processes of these PAHs [6,7] may be involved. Many processes have been considered in the literature as detailed in the review of Wang [8] or more recently in the paper of Frenklach and Mebel [9] who extensively described the latest efforts of nucleation modeling in order to define criteria to be matched by a nucleation model and finally to propose a two-step H-abstraction-C-addition (HACA) driven model fulfilling them.

In order to better understand the chemical and physical processes involved in the nucleation step, there is a need of dedicated experiments allowing scrutinizing this transition. Many detailed flame structure

studies have been provided in the literature and constitute reference databases for assessing kinetic mechanisms of polycyclic aromatic hydrocarbons (PAHs) and soot formation. For instance soot formation was studied by exploring sooting flame conditions with equivalence ratio generally greater than 2 for a large variety of fuels including alkanes [10–19]. Other experiments were focused on the understanding of the chemistry of rich non sooting flames [20–22]. The chemical mechanisms of fuel decomposition and small aromatic hydrocarbon formation in fuel-rich flames were described in a review article by K. Kohse-Hoïnghaus and coworkers [23]. All these studies have contributed to improve significantly the kinetic modeling in near-sooting or sooting conditions. However, the ultimate accomplishment still requires a better description of the nucleation process.

Recently the existence of nucleation flames, burning different fuels and at different pressures, in which soot particles undergo negligible growth with residence time in the flame, has been demonstrated [24–28]. In these flames, the soot particles remain at constant diameter around 2-4 nm along the height above the burner (HAB) [27] and the soot volume fraction increases mainly by its number of smallest measurable soot particles, which are issued from the overall nucleation process [26]. Thus nucleation flames are of great interest to gain insights into the soot nucleation step and for the development and validation of soot nucleation models [4,26,29,30].

The objective of this work is to provide a detailed experimental database intended to better understand the soot nucleation and to use it to assess the strengths and weaknesses of soot models currently used in the combustion research community. The study focused on the chemical analysis of three premixed atmospheric n-butane/oxygen/nitrogen flat flames covering equivalence ratios ϕ from 1.60 to 1.95. The flame at ϕ = 1.60 (Flame1.60) is a rich non sooting flame. The flame at ϕ = 1.75 (Flame1.75) is a nucleation flame. The flame at ϕ = 1.95 (Flame1.95) is a lightly sooting flame. The soot volume fraction (SVF) profiles and their size distributions were previously measured in Flame1.75 and Flame1.95 [27,31]. SVF was shown to increase in the burnt gases from around 0.1 ppb in Flame1.75 to 10 ppb in Flame1.95 [31]. Thus, these flames cover a range of soot volume fractions much weaker than found in the literature but are particularly well suited for scrutinizing the nucleation step. The fuel under investigation is n-butane. It is a major component of Liquefied Petroleum Gas and it exhibits oxidation behavior similar to that of larger paraffins found in gasoline [32]. Its oxidation has been widely studied in K. Kohse-Höinghaus group [33] and well represented by detailed [33-35] and reduced chemical mechanisms [36].

In the present study, additional data are provided. Mole fractions of stable species up to benzene were measured by gas chromatography (GC) while naphthalene and pyrene were obtained by jet-cooled laser induced fluorescence (JCLIF). The flame temperature profile was determined by LIF thermometry applied on NO species. Temperature profiles provided in [27] are completed here for Flame1.60. The mole fraction profiles reveal a high sensitivity of a few species with equivalence ratio, particularly

acetylene, propyne, benzene, naphthalene and pyrene species whose increase is expected to explain the observed two order of magnitude soot volume fraction increase.

To complete this study, the cases were simulated using three kinetic mechanisms of the literature coupled to a soot model based on a sectional approach [29]. This soot model has been chosen because its description of the soot formation and growth processes is representative, independently of the distribution representation method (sections or moments), of the models vastly used in current computational fluid dynamics (CFD) attempts to model soot and particles distributions [37-39] as well as the models used in 0D/1D cases where all steps of soot formation and growth are modeled and the gas and soot phases are fully coupled [40-42]. In addition to the assessment of the model capability to predict soot volume fraction and distributions, this last part will therefore serve two purposes. First, it will allow to assess the ability of such soot model to predict soot with a prediction of gas phase species, PAH included, thanks to the experimental results provided in the first part. Second, it will provide insights on the progress to be made by this type of model to predict particle size distributions accurately.

2 Experimental

2.1 Selected flames and burner

Experiments were performed in three atmospheric n-butane/oxygen/nitrogen premixed flames in order to span a wide range of equivalence ratios for testing the robustness of the modeling. The soot measurements were previously performed in the two sooting flames Flame1.95 and Flame1.75 [27,31]. Flame1.60 (ϕ = 1.60) is a blue color rich non-sooting flame (soot particles could not be detected by laser-induced incandescence (LII) or scanning mobility particle spectrometer (SMPS)).

The flame conditions were initially selected [27,31] to obtain a nucleation flame, with the specific sooting behaviour feature depicted in the introduction, and presenting good stability and reproducibility. These characteristics could be observed in a small range of equivalence ratios [1.70-1.75], by imposing a dilution ratio of 55.4% and a total mixture flow rate of 6.71 standard litre/minute (273 K and 1 atm). The equivalence ratio 1.75 was finally selected because it provides a better signal-to-noise ratio. As will be shown later, these nucleation flame conditions imply that its flame front is very close to the burner surface, by contrast to the low pressure nucleation flame [26]. This drawback prevented a satisfactory experimental investigation of the flame front region, while data obtained downstream of the flame front were found very reliable. For reasons of consistency, the two other flames Flame1.95 and Flame1.60 kept the same dilution and total flow rate as the Flame1.75.

Experimental flames conditions are summed up in Table 1. The absolute uncertainty on the equivalence ratio is estimated to ± 0.02, considering the mass flowmeters precision.

	Φ	C/O	$X_{c_4H_{10}}$	X_{O_2}	X_{N_2}
Flame1.95	1.95	0.60	10.30%	34.31%	55.39%
Flame1.75	1.75	0.54	9.46%	35.22%	55.32%
Flame1.60	1.60	0.49	8.81%	35.86%	55.32%

Table 1 Flames conditions. Total flow rate: 6.71 L/min STP.

The flames were stabilized on a 60 mm-diameter bronze porous Holthuis burner surrounded by a shielding co-flow of nitrogen set at 20 SLPM. A water-cooling circuit keeps the burner temperature at 70°C during experiments. A stainless-steel disk (60 mm diameter, 30 mm thick) is placed at 16 mm above the burner surface to ensure the good flame stability. For on-line measurements, the disk is perforated at its center for introducing axially sampling microprobes. Two kinds of microprobes were used in order to measure (1) the mole fraction profiles of the stable gaseous species by GC and JCLIF and (2) the soot size distributions by using SMPS. It is noteworthy that the intrusive microprobes may perturb the measured profiles (see Section 3.1) [43]. This effect is hardly quantifiable mostly in the reaction zone, i.e. below 2 mm.

2.2 Temperature measurements

In this work, the temperature profiles along the flame centerline were obtained by multiline laser-induced fluorescence thermometry on NO species. Temperature profiles in Flame1.95 and Flame1.75 were already provided in [27] and are completed here in Flame1.60. The setup and the data analysis procedure are detailed in the supplementary information of [27] and in [44]. The laser system consisted of a frequency-doubled Nd:YAG-seeded laser (SLM Q-smart 850) pumping a dye laser (Quantel TDL+). The narrow laser bandwidth (0.2 cm^{-1}) allows to reduce the spectral range of the LIF excitation spectra to [225.3 - 225.35] nm similarly as in [45]. Temperature was determined from the least mean square between the experimental and the simulated spectra library generated using LIFBASE [46]. The temperature uncertainty is estimated to be ± 80 K in the burnt gases [27]. The temperature at 16 mm corresponds to the plate temperature measured with a K-type thermocouple. The experimental temperature profiles show that the flames are stabilized very close from the burner surface with a maximum between ~ 1 and 2 mm. In these conditions, it was not possible to measure the temperature gradients with our experimental set-up due to the beam steering below ~ 1 mm, but it was estimated from calculation. The resulting temperature profiles are given in the supplementary material SM1.

2.3 Gaseous species measurements

The aliphatic compounds and aromatics mole fraction profiles were measured by on-line GC and JCLIF. The sampling of these species was ensured thanks to a quartz microprobe (200 µm tip aperture, ended by a 20° conical aperture, 100 µm positioning accuracy) connected to a heated line (T=100°C) and kept at sub-ambient pressure (400 - 500 Torr) to reduce condensation and adsorption of water and high molecular weight compounds on the probe wall. The sampling line is connected to the GC and JCLIF apparatus described below. The distance between the burner surface and the tip of the microprobe can be modified by changing the position of the microprobes with respect to the position of the burner at different height above the burner (HAB).

- *Aliphatic compounds and benzene mole fraction measurements by on-line GC*

The mole fraction profiles of O_2, CO, N_2, several aliphatic compounds (from ethylene to 1-butyne) and benzene have been determined using GC analyzer (Varian CP-3800). Aliphatic compounds and benzene were analysed with a HP-Plot Al2O3 capillary column (Ø 0.32 mm) and a flame ionisation detector (FID). Two isometric forms of C_4H_6 were measured: 1-butyne and 1,3-butadiene. O_2, CO, N_2 were separated in a molecular sieve 5A column (Ø 0.53 mm) and detected with a thermal conductivity detector (TCD). Helium was used as a carrier gas. The species were directly calibrated using gas cylinders of known concentration. The threshold of detection of most species by GC was experimentally determined around 0.2 ppm.

- *PAH mole fraction measurements by JCLIF*

Mole fraction profiles of naphthalene and pyrene were determined by JCLIF, which is a method specifically developed for the selective and quantitative PAH measurements in flames, as detailed in previous papers [47–49]. This technique relies on the microprobe extraction of the species from the flame and their drastic cooling (around 100 K) inside a free jet expansion generated in an ultra-low-pressure analysis chamber, where the species are directly excited by using a tuneable laser pulse. Under such low pressure and temperature conditions, it has been demonstrated in previous works [48-50] that the measured excitation and fluorescence spectra of the sampled species provide sufficiently resolved and distinctive spectral features for the selective detection of naphthalene and pyrene notably. This method indeed offers a dual selectivity for the species measurement provided by the careful adjustment of the laser excitation wavelength on a specific absorption band of the naphthalene or pyrene species and the judicious selection of the collection fluorescence spectral range for each species. Moreover, fluorescence lifetimes of the excited species, which are controlled during these experiments, are characterised under free collision regime by specific and clearly distinguishable values, almost unique for each PAH, providing another guarantee of the correct selectivity of the measurements.

The pressure inside the line was kept constant to 10 torr (13.33 mbar) thanks to a regulated motorized valve. The laser system consisted of a frequency-doubled Nd:YAG laser pumping a dye laser in order to generate tuneable laser pulses in the UV domain after frequency doubling. Naphthalene and pyrene were respectively excited at fixed wavelengths around 308 nm and 321 nm. The laser beam was sent into the analysis chamber unfocused and spatially reduced (diameter approximately 1 mm) with a pinhole. The laser energy was adjusted to approximately 0.05 J/cm^2 to be in the linear regime of fluorescence. Fluorescence signals were recorded with a photomultiplier (Photonis XP2020Q) via an Acton 2300i spectrometer (300 mm focal length - 1200 g/mm grating). Mole fraction profiles were determined according to a two steps procedure. LIF profiles were first recorded along HAB before being calibrated into absolute mole fraction profiles using known amounts of naphthalene and pyrene and according to a similar procedure as described in [49-50].

2.4 Soot particles measurements

The soot volume fraction profiles were previously obtained by using laser-induced incandescence (LII) calibrated by the extinction-based method cavity ring-down extinction (CRDE) [31]. In addition, the soot size distribution was determined by combining SMPS, time-resolved LII and helium ion microscopy (HIM) [27]. The particle size distribution functions (PSDF) measurements were carried out using (1) online size distribution analysis of microprobe-sampled particles using a 1 nm-SMPS and (2) ex situ analysis by helium-ion microscopy (HIM) of particles sampled thermophoretically. The diameter of the smallest soot particles detected by 1nm-SMPS and HIM was also found in good agreement with the one determined by time-resolved LII [27].

The results obtained by LII and HIM are directly transposed here respectively from [31] and [27] without modifications. They are summarized in the supplementary material SM2 and presented in several figures in this study. On the contrary the initial PSDFs measured by SMPS in [27] were not corrected for some flaws. This is accomplished in the present work as detailed below. The corrected PSDF then serve as a database for modeling.

The PSDFs can be fitted with a log-normal distribution:

$$f(D_p) = \frac{1}{D_p\sqrt{2\pi}\ln(\sigma_g)} \exp\left[-\left(\frac{\ln\left(\frac{D_p}{D_g}\right)}{\sqrt{2}\ln(\sigma_g)}\right)^2\right] \qquad \textit{Eq. 1}$$

where D_p is the primary particle diameter, D_g is the geometric mean primary particle diameter of log-normal distribution and σ_g is the geometric standard deviation of D_p.

The measurement of the size distribution of nanometric soot particles has become accessible thanks to scanning mobility particle spectrometers [51,52]. The 1nm-SMPS used in this work is the Model 3938E77, TSI Inc., Shoreview, MN, USA. The PSDFs of the mobility diameter measured with the 1nm-

SMPS in Flame1.75 presented in [27] are raw data. The raw mean geometric mobility diameters were found to be respectively 3.37, 3.09 and 2.97 nm at 10, 8 and 6 mm in Flame1.75 (Fig. 1).

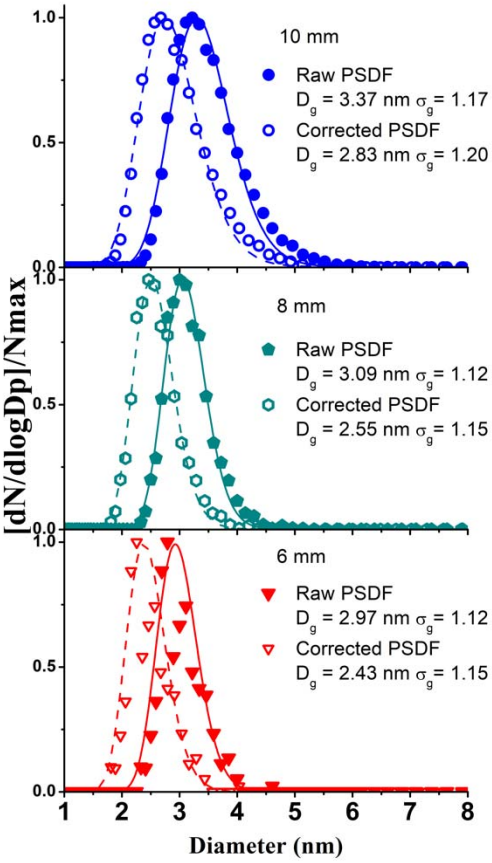

Figure 1 The normalized PSDF (raw [27] and corrected (this work)) of the diameter measured by 1 nm-SMPS at 6, 8, and 10 mm in Flame1.75. The filled and empty symbols are respectively raw and corrected data from nanoparticle transport theory [53]. The lines are fits to data using a lognormal distribution function and the corresponding fitting parameters are shown in the figure.

These raw SMPS PSDFs are potentially subject to two main uncertainties:

(a) according to the literature [54] the mobility diameters D_m can overestimate the particles diameters smaller than 10 nm because SMPS commercial software uses the empirical Cunningham slip correction. This correction does not account [55,56] for (1) the transition from diffuse to specular scattering, and (2) the van der Waals gas–particle interactions; both effects are expected to be important for nanoparticles. Thus, Abid et al. [53] proposed a correction function for soot, deriving from a nanoparticle transport theory where these interactions are accounted for, it reads:

$$D_p = D_m \times \tanh(1.4566 + 0.010892 D_m) \times \left(1.0721 - \frac{0.4925}{D_m}\right) \qquad \textit{Eq. (1)}$$

with D_p the particle diameter and D_m the mobility diameter in nm.

The application of this correction on the raw PSDFs induces a shift toward lower diameters with mean particle diameters of 2.83, 2.55 and 2.43 nm respectively at 10, 8 and 6 mm. Corrected particle size distributions are shown in Fig. 1. These new distributions will be considered in this work.
(b) the second source of uncertainty on these raw PSDFs is due to diffusion losses. The diffusion losses impact the measured soot concentration and the shape of the PSDFs. These losses occur when particles collide and cling to the surface due to van der Waals and electrostatic forces and surface tensions. Diffusion losses are unavoidable during the soot sampling. They are important, especially for particles below 10 nm. Their quantification remains complex considering all sources of loss along the sampling line. Thus, the TSI "Aerosol Instrument Manager" software (AIM) proposes a correction function for diffusion losses which occurs only within the SMPS. This correction is considered in numerous papers [13,53,57-59]. However, the correction function is not yet reliable for particles below 3 nm. The absence of diffusion losses correction induces a potential underestimation of the particles number below 10 nm. The reported PSDFs in this work were obtained by HIM and SMPS in Flame1.75 and by HIM in Flame1.95. Note that the PSDFs obtained by HIM are also subject to uncertainties, as explained in the supplementary material SM2. For example, the adhesion efficiency of smaller soot particles collected on silicon wafers is lower than that of more mature soot [51,60]. This leads to an underestimation of their number relatively to more mature soot particles. This especially occurs at 6 and 10 mm in Flame1.95, where both very small and larger soot particles coexist [13]. A possible consequence is an alteration of the shape of the PSDF in Flame1.95 with an attenuation of the contribution of the smallest particles.

The above drawbacks affecting PSDFs determined by HIM or SMPS mainly alter the quantitative potential of the used techniques for determining the total number of particles. This disadvantage is circumvented here since in this work only the size distributions are extracted from SMPS and HIM measurements while the soot volume fraction is directly calibrated in situ using CRDE.

2.5 Experimental results

Table 2 summarizes the different scalars measured in this work as well as the experimental techniques, sampling methods, detection threshold, vertical resolution and accuracy. The purpose of this table is to aid in the comparison of experimental data with numerical data. Among the measured mole fractions profiles, all provided in the supplementary materials SM3 (SM3_DATA_FLAME_1.60, SM3_DATA_FLAME_1.75, SM3_DATA_FLAME_1.95), Fig. 2 and 3 show those presenting a mole fraction variation greater than 5 in the burnt gases within the investigated equivalence ratio range [1.60

– 1.95]. These species are acetylene, propyne, butyne and benzene measured by GC and naphthalene and pyrene measured by JCLIF. The mole fraction of these two PAHs was too low to be measured in Flame1.60.

Measured scalar	**Experimental technique**	**Sampling method**	**Detection threshold**	**Vertical resolution**	**Accuracy**
Gas temperature	Multiline NO-LIF thermometry	In-situ	-	0.8 mm	± 80 K
Mole fraction	GC	On-line	0.2 ppm	0.4 mm	3 % C_2H_2 2% C_3H_4 13% C_4H_6 10 % for benzene
	JCLIF	On-line	10 ppb	0.4 mm	± 30 %
Soot volume fraction	LII calibrated by CRDE	In-situ	10 ppt	0.48 mm	± 45 %
PSDF	HIM	Ex-situ	Particle diameter 1 nm	2 mm	± 0.6 nm
	SMPS	On-line	Mobility Particle diameter 1 nm	0.2 mm	Undetermined

Table 2 Summary of the different measured scalars, the experimental techniques, sampling methods, detection threshold, vertical resolution and accuracy used in this work.

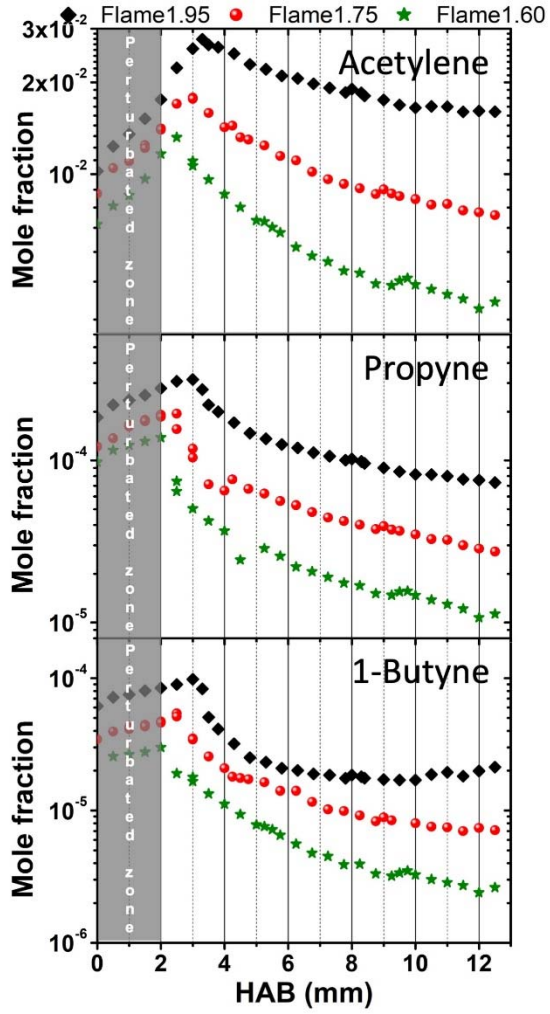

Figure 2 Profiles of selected aliphatic compounds: acetylene, propyne and 1-butyne, measured by GC in the flames at Φ =1.60, 1.75 and 1.95.

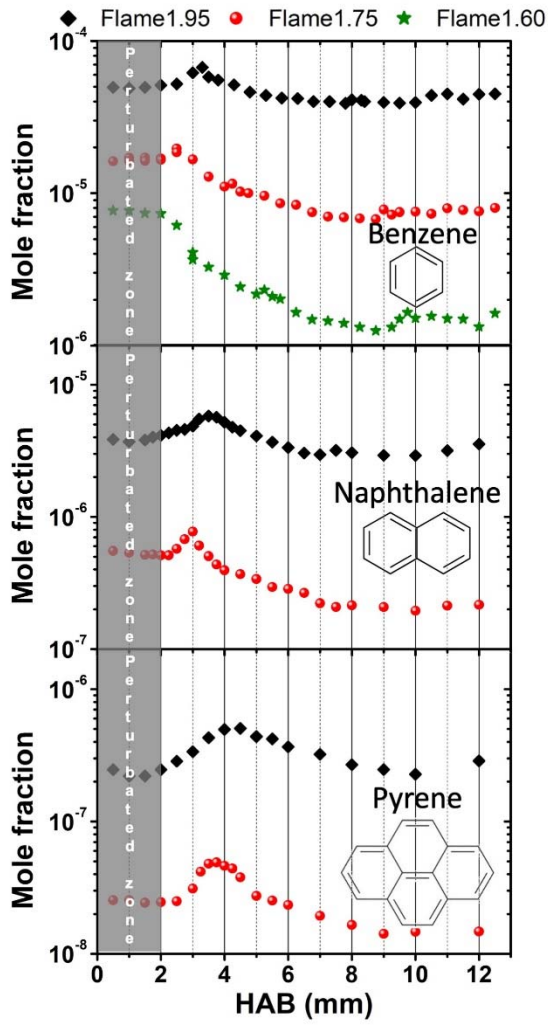

Figure 3 Profiles of aromatic compounds measured by GC (benzene) and JCLIF (naphthalene and pyrene) in the flames at Φ =1.60, 1.75 and 1.95.

It turned out that an important reactivity at low HAB occurred due to the proximity of the flame front from the burner surface. This results in a significant consumption of n-butane from the burner surface (supplementary materials SM3). Such reactant consumption was observed in few studies like [10,15,61] in atmospheric flames stabilized on porous burners. The early reactivity also induces an important concentration near the burner surface of intermediate species sampled by microprobe as also observed in [11,62-69]. Therefore, caution must be undertaken in the interpretation of the profiles upstream 2 mm, materialized by the grey zone on the figures. In addition, the species profiles measured after probe sampling are probably shifted towards the burnt gases with respect to the soot profile (Fig. 4) determined by in situ LII measurements. Indeed, the soot onset in Flame1.95 is located at 3 mm i.e. 1 mm upstream the peak of pyrene. One would expect that the consumption of soot precursors, including pyrene, might be correlated with the soot onset. This concordance was particularly observed in low pressure sooting flames [26] in which the higher distance of the flame front stabilization with respect to the burner surface

and the less sharp temperature gradient certainly minimize the drawbacks evocated above in our atmospheric pressure flames.

It is to be noted that the aliphatic compounds profiles measured in this work follow a progressive sequence characteristic of the fuel-rich chemistry of alkanes described in [23]. For example, the consumption of intermediate species, ethylene, propene, butene and butadiene (data in the supplementary materials SM3) occurs upstream of the peak of formation of acetylene, propyne and 1-butyne. An illustration of this sequence is given in the supplementary material SM3 in case of Flame1.75. This observation is consistent with the reactions of transformation of alkene in alkyne species. Then, it is also interesting to highlight that the benzene profiles peak at the same position than the profiles of acetylene (C2), propyne (C3) and butyne (C4). This observation is consistent with the involvement of C2, C3 and C4 in the benzene formation through the reactions C2 + C4 and C3 + C3 described in [12,23,70-72]. Moreover the benzene profiles in Fig. 3 in sooting flames peak before the naphthalene profiles which peak before pyrene profiles. The change in location of peak of benzene, naphthalene and pyrene could be due to sequential molecular growth. Finally, it is noteworthy that all these species persist in the burnt gases and that their concentration increases with the equivalence ratio.

The soot volume fraction profiles, PSDFs and HIM pictures in the two sooting flames are shown in Fig. 4. For each flame, the gain of the PMT detectors used for LII measurements was adjusted in order to increase the signal to noise ratio while avoiding the PMT saturation due to the continuous flame emission which is much higher in Flame1.95 than in Flame1.75. The 20-ms aperture chopper, interposed on the LII collection path, significantly reduces the emission of Flame1.95 but not sufficiently to achieve the similar sensitivity as in Flame1.75 [27]. The soot onset is defined here by the first measurable LII signal in each flame. Despite their very small size (2-4 nm), these smallest incandescent particles were found to have optical properties close to those of mature soot, although 40% less absorbing [31], and are described as primary particles monomers in [74]. In Flame1.95 the soot onset appears at 3 mm with a soot volume fraction of ~380 ppt. Then the soot volume fraction f_v increases by a factor 25 until approaching a plateau above 10 mm. This rise is due to the increase of the number of soot nuclei but also to the activation of the growth process due to condensation and surface growth reactions. This is well illustrated on the HIM PSDFs evolution, which shows an increase of the mean particle diameters from 4.8 to 10.6 nm with HAB. From 6 mm, the aggregation process is observed on the HIM pictures starting with aggregates of 2-3 primary soot particles and becoming slightly larger with the HAB. Unfortunately, the contrast is too low on the pictures to proceed an analysis of the soot fractal dimension. The aggregation process is found concomitant with the nucleation, coagulation and growth processes. In Flame1.75, the soot onset is starting from 5 mm with a soot volume fraction of ~10 ppt. Then the soot volume fraction f_v increases by a factor of 7 over 7 mm, while accompanied by a weak evolution of the PSDFs with a mean diameter of D_m evolving from 2.4 to 2.8 nm with HAB. The HIM images at 12 mm

do not reveal the existence of aggregates. This behaviour characterizes the so-called nucleation flame [24,25,27].

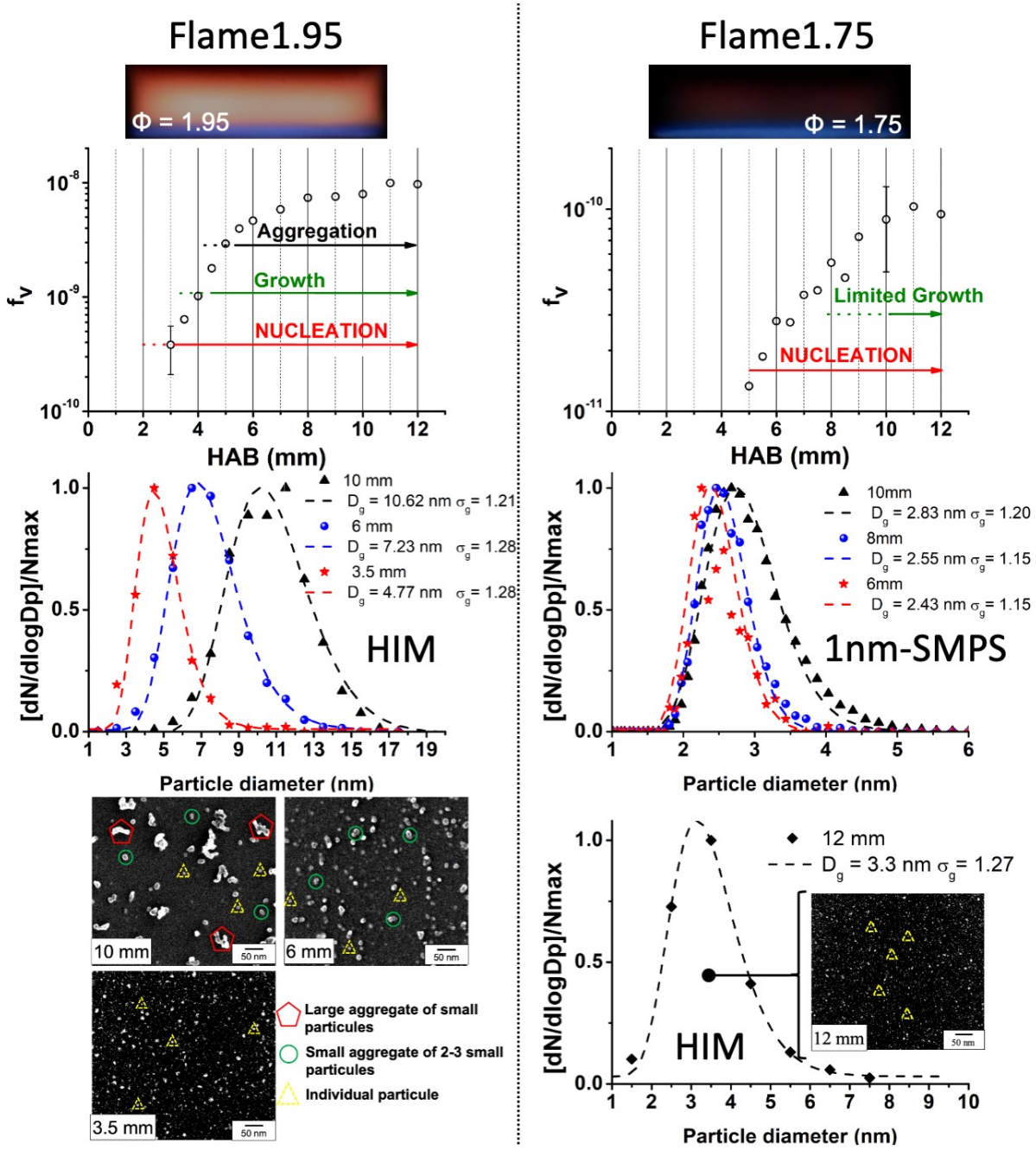

Figure 4 Soot volume fraction profiles f_v , HIM and/or 1nm-SMPS PSDFs and HIM pictures in Flame1.95 (left column) and Flame1.75 (right column) previously measured in [27,31]. Soot formation steps are schematically represented on the f_v profiles as function of HAB in each flame. The dashed lines are fits to data using a lognormal distribution function whose corresponding fitting parameters are

indicated in the inset. The spatial resolution of HIM measurements due to the sampling procedure is ± 1 mm (see supplementary material SM2). That of the SMPS measurements could not be estimated.

3 Comparison with flame modelling

Flame modelling has been performed for the purpose of showing the unique interest of the present studied target flames and how they could permit to evaluate PAH-soot interaction models (particle inception, adsorption, desorption) that were lacking proper validation so far because of the scarcity of experimental data. In this context, three chemical mechanisms have been selected. These mechanisms have been coupled to a soot model recently developed with an emphasis on the interaction between PAH and soot phase [29,75]. As mentioned in the introduction, this mechanism is considered to be representative of what is used by the soot modelling community for simulations of sizes from academic laminar burners [40-42] to much 3D turbulent setups [37-39]. All the presented simulations were performed using the kinetic solver Cantera [76]. While the analysis of the reaction pathways of PAH formation through these three mechanisms is beyond the scope of this work, the use of three different mechanisms for the gas phase and the various parameters used for soot modelling pointed up numerous aspects of PAH and soot modelling which could be improved and for which experimental results presented above will be very valuable to assess the performance of future models. The section begins with a brief description of the gaseous species prediction given by each mechanism. Then the soot results obtained by coupling the chosen soot model with each mechanism are compared with each other and with the experimental measurements, setting a baseline for further parametric variations. From this baseline, a variation of the PAH adsorption/desorption model is presented to highlight the importance of this process and how it interacts of the particle inception model. Finally, these conclusions about the PAH adsorption/desorption model will allow to confirm, based on comparison with experimental measurements, the importance of the recent works on particle inception modelling.

3.1 Gaseous species modelling

The three selected chemical mechanisms will be referred as U.Lille, KAUST and POLIMI hereafter. U.Lille was developed for n-butane oxidation in sooting flame conditions [44]. It originates from a previous mechanism [77] used to model the formation of the first aromatic ring and PAHs (naphthalene and pyrene) produced in low pressure rich fuel methane flames. It includes 279 chemical and 1423 elementary reactions and is available in [44]. KAUST is a kinetic model for the gasoline surrogate mixtures, developed to predict the fuel oxidation along with the formation of PAHs and soot in flames. This model was tested against ignition delay times and laminar burning velocities. It includes the formation and growth of PAHs up to coronene. The high temperature version includes 574 species and 3379 reactions and is available in [78]. POLIMI is the detailed/lumped mechanism of the pyrolysis, partial oxidation and combustion of Primary Reference Fuels, including PAH formation up to C20. The high temperature kinetic scheme PRF_PAH_HT_1412 contains 176 species and 6067 reactions and is

available online (http://creckmodeling.chem.polimi.it/index.php). It was tested in a large range of experimental data [79-82].

The three kinetic mechanisms U.Lille, KAUST and POLIMI were used to predict the main chemical structure of the three rich flames of n-butane. In this section, the mechanisms are used without soot model. Temperature profiles were imposed for these simulations. These profiles are given in supplementary materials SM1 and have been obtained following the approach proposed by Bejaoui et al. [83], notably combining the temperatures calculated by solving the enthalpy equation in the gaseous domain with the experimental ones measured at the stabilization plate location, in order to rebuilt the temperature profiles in each flame. These rebuilt temperature profiles fit satisfactorily the temperatures measured by NO-LIF thermometry.

The comparison between the predicted and the experimental mole fractions of acetylene, propyne, 1-butyne, benzene, naphthalene and pyrene is presented here. These six species were selected because of their significant variation with the equivalence ratio (Fig. 2 and 3) and their influence on soot formation pathways. The other measured species profiles (n-butane, oxygen, carbon monoxide, nitrogen, methane, ethane, ethylene, propane, propene, allene, buta-1,3-diene, vinylacetylene, trans-2-butene, cis-2-butene, but-1-ene, isobutene) are provided in the supplementary materials SM3.

Figure 5 shows the comparison between the predicted and the measured mole fraction profiles of C_2H_2 in Flame1.60. The C_2H_2 profiles of Flame1.75 and Flame1.95 are provided in SM3. The value of the peak mole fraction is well predicted in each flame by the three models. However, the experimental peak value of C_2H_2 is shifted by around 1.7 mm towards the burnt gases in comparison with the predicted peaks. This shift is attributed to the disturbance induced by the sampling, reinforced in the vicinity of the burner surface, as previously underlined in several works [84-86]. Assuming this shift affects similarly all the species profiles measured after probe sampling, we have applied in the following, a systematic shift of 1.7 mm to all the experimental profiles of gaseous species.

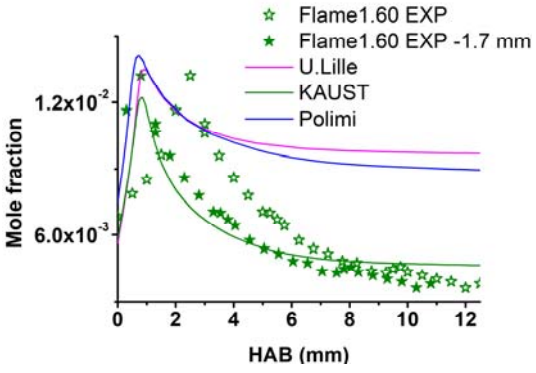

Figure 5 Comparison between the predicted (lines) and the measured (symbols) mole fraction profiles of C_2H_2 in Flame1.60. Closed symbols represent the experimental data (open symbols) shifted by 1.7 mm towards the burner surface.

The comparison of the mechanisms predictions and (shifted) measurements is presented at the peak mole fraction in the flame front and in the burnt gases at HAB = 8 mm. Results for acetylene, propyne and 1-butyne are summed up in Fig. 6 while Fig. 7 collects those for benzene, naphthalene and pyrene. Due to the absence of a predicted peak of naphthalene and pyrene in the flame front of the flames with POLIMI simulations, the reported peaks values in Fig. 7 are taken at 2 mm. The experimental and modeled profiles of C_2H_2 and pyrene are available respectively in Fig. 5 and Fig. 9. For a complete description of the four other selected species evolution, their profiles (experimental and modelled) are also provided in the supplementary materials SM3.

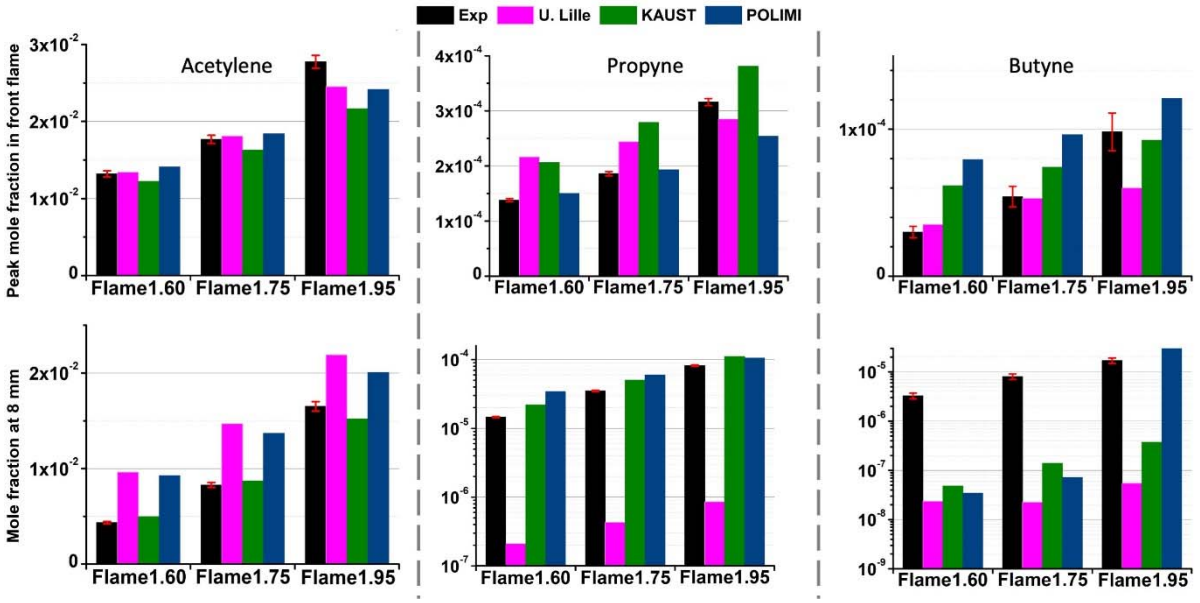

Figure 6 Comparison of the mechanisms predictions (U.Lille; KAUST and POLIMI) and measurements (black) at the peak mole fraction in the flame front (top row) and at 8 mm (bottom row) for acetylene, propyne and 1-butyne. Note that linear and logarithmic scales are used.

The acetylene predictions for the three mechanisms are in very good agreement with the experimental measurements in the flame front. In the burnt gases the deviations which reach a factor of two in Flame1.60 decrease below 35 % in Flame1.95. In case of propyne species, the KAUST and POLIMI mechanisms reproduce the dynamic over the three flames within 30 % while the U.Lille mechanism significantly underpredicts the burnt gases mole fractions. Although a persistent level of a few ppm of 1-butyne is measured in the burnt gases of all flames, each mechanism underpredicts it by around two orders of magnitude.

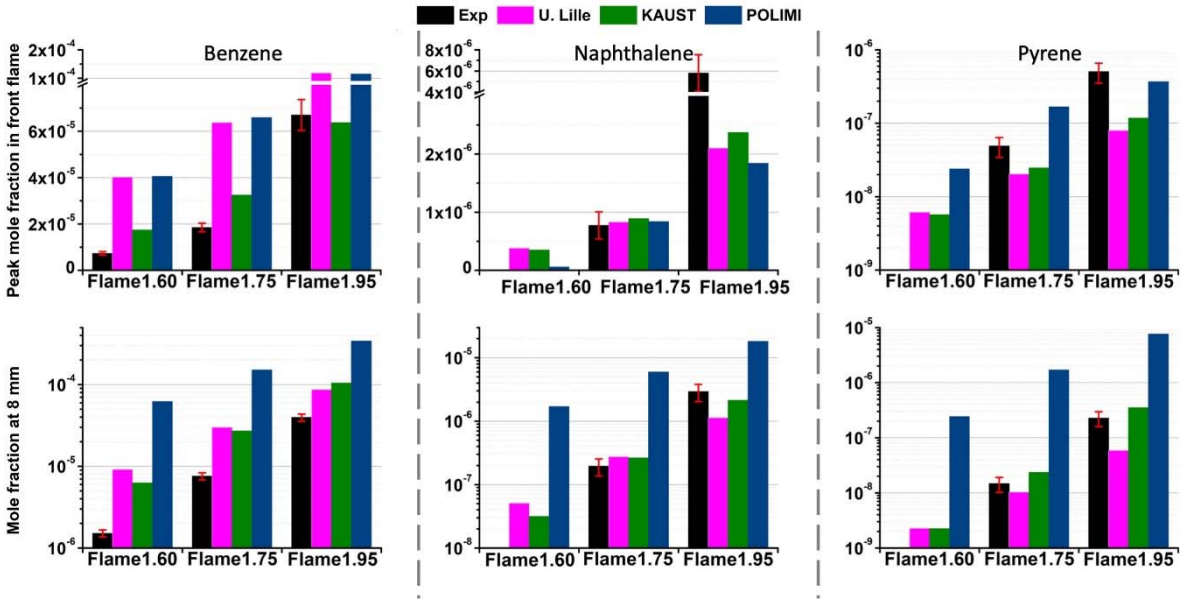

Figure 7 Comparison of the mechanisms predictions (U.Lille, KAUST and POLIMI) and measurements at the peak mole fraction in the flame front and at 8 mm for benzene, naphthalene and pyrene.

Globally each mechanism reproduces well the significant increase of the aromatic species mole fraction with the equivalence ratio, as observed experimentally (Fig. 7). Regarding the peak mole fraction value in the flame front region, we recall that it can be affected due to the reactivity near the burner surface as explained previously. Each model overestimates the benzene mole fraction in the flame front especially in the richer flame where the disagreement exceeds one order of magnitude. On the contrary, the overestimation of the benzene mole fraction in the burnt gases tends to be reduced by a factor 5 in Flame1.60 to less than 30 % in Flame1.95 for U.Lille and KAUST, while the overestimation with POLIMI remains larger in each flame which seems understandable since this mechanism also exists in a version with a soot model consuming PAHs (not used presently because another soot model is used in the following). Concerning the two measured PAHs, it is reminded that the experimental detection threshold of naphthalene and pyrene is around 10^{-8}. While naphthalene JCLIF signals could be identified in Flame1.60, the signal to noise ratio was too low for accurate interpretation. The predictions of naphthalene and pyrene are satisfying in the burnt gases, except for POLIMI which overestimates the mole fractions by at least one order of magnitude in all flames. However, it should be noted that the POLIMI mechanism assigns the $C_{16}H_{10}$ structure to a single species, namely pyrene, which may partly explain the mentioned overprediction. Regarding the peak mole fraction of naphthalene, a very good

agreement between the predictions and the measurements is found in the nucleation Flame1.75 while the models underestimate the peak value by a factor 3 in Flame1.95. The particular case of pyrene predictions is discussed in detail in the soot modeling section.
Overall, the KAUST mechanism gives the most satisfactory results on a wide range of species involved in the PAH and soot formation process.

3.2 Soot modelling

The results presented in Section 2.5 permits the evaluation of all aspects of a soot model as well as the gas-phase mechanism it is coupled with. The next step of this evaluation is to couple the soot model based on a sectional approach proposed in Aubagnac-Karkar et al. [29] with the three mechanisms (U.Lille, KAUST, POLIMI) for the simulation of the three flames presented above. As in [29], 70 sections have been used for all simulations to discretize the particle size space. A reference parameter set, described below, has been used to obtain baseline results from which parametric variations are then performed. These variations emphasize the influence of some specific points such as the reversibility of condensation (thus modelling PAH adsorption and desorption), the choice of the precursors depending on the mechanism or the ability of the model to predict the smallest particles accurately. As explained previously in this paper's introduction and at the beginning of Section 3, the conclusions of this section are expected to be general enough to be applied to most similar scale models.

The soot model takes into account the five main phenomena driving soot particles formation and evolution: particle inception from PAH collisions, growth by PAH adsorption represented by PAH collisions on soot particles, soot particles coagulation and the soot surface chemistry with oxidation and surface growth reactions. Soot surface chemistry is based on the HACA cycle with parameters described in Appel et al. [87] coupled to the soot phase as in Aubagnac-Karkar et al. [75]. The other three phenomena are modeled based on Smoluchowski equation [88]. Particle inception and condensation sub-models include some specific development which are described in [29] and briefly recalled in this section.

In the reference parameters set, pyrene is used as the only precursor for nucleation and condensation. As mentioned in several studies [3,89-93], pyrene dimerization is very unlikely to be the source of actual particles. However, soot inception is still not understood. It was expected to be related to larger species which appear further in the flame [5–9], but recent studies linked it to more complex species created by combination of small to moderate sized PAHs [3–5] potentially leading to the formation of bridged dimers of PAHs [6,7]. Moreover, these progresses rely only advanced modelling, never validated with a complete and larger scale model (in the sense of modelling all processes and coupling with gas phase) neither against any experience (for the obvious reason of the scarcity of such data). Therefore, pyrene is here used as a precursor because it allows its comparison against experiment

and, if not directly involved in soot nucleation, it is still considered to be related to the gas-phase growth of actual precursors [3]. Moreover, not all of the considered mechanisms include PAH larger than pyrene. Pyrene has been shown in numerous previous studies that it was a species close enough to actual precursors to give good tendencies [1,26,28,29,75,94-98]. Thanks to the experimental data provided in the previous sections, the influence of this simplifying assumption is evaluated in Section 3.3 with the introduction of cases using all PAH larger than pyrene for particle inception and PAH adsorption/desorption in the cases using the KAUST mechanism.

Soot-PAH interactions are complex and cannot be precisely described in a simplified model used in flame simulations where the soot concentration can exceed 10^{11} particles per cubic centimeter [13], a concentration too large to be described more precisely than with global statistics. Potential PAH can be adsorbed but also desorbed depending on the temperature and particle structure [99-101]. In the chosen model, all these possibilities are gathered into a single reversible process whose forward rate is the number of PAH-soot collision and backward rate is computed based on the forward rate and an equilibrium constant evaluated using a relation given in Totton et al. [102]. The complete description of this PAH adsorption/desorption model and its standard parameterization are given in [29], where it is referred as "reversible condensation". The resulting particle inception model is based on PAH collision dampened by a factor, such as a collision efficiency but computed based on an equilibrium constant as well. In the following, the soot model parameters will be the same as the ones used in [29] unless stated otherwise. The value of the intermolecular vibrational wavenumbers $\lambda_{i,cond}$, involved in the computation of the condensation equilibrium constant, was lowered (from 7 cm^{-1} [29] to 5 cm^{-1}) because the default value overproduces pyrene in Flame1.95. This modified value of $\lambda_{i,cond}$ has been applied for every simulation presented thereafter. This value remains within the range found in the literature [8,103] and is acceptable considering the simplifications of the model.

The proportion of reactive active sites, represented by α_{HACA} in the model, is the only parameter that must be adjusted between the different flames as in the reference work. This parameter is usually used to correct known uncertainties on soot chemistry as in [19,29,94,98,104]. Having to change this parameter indicates that either the way the surface chemistry is integrated in the model or the chosen surface chemistry mechanism, lacks the ability to describe soot interactions with light gas species in the conditions explored in this previous study (critical equivalence ratios where soot particles are first detected). Although it stresses a flaw of the model, this also shows the interest in studying these specific conditions to improve the understanding of soot formation. Various strategies have been proposed in the literature that can improve predictivity of the model in these cases, including Arrhenius coefficients depending on particle size [105-107], following particles thermal history to adapt surface activity [104], or extending the surface chemistry mechanism [108-109]. In the present work, because of the significant difference between the experimental measurements of pyrene and the different predictions provided by the three mechanisms, α_{HACA} is only used to adjust the calculated soot volume fraction to a value close

to the one experimentally measured in Flame1.75 and Flame1.95, so that the conclusions driven on PAH-soot interaction are not perturbed by a too large error on soot volume fraction while the nucleation and condensation modelling parameters remain the same in all simulations. Hence, in this work, we have simply considered the parameter α_{HACA} as an adjustment value for the simulation.

The values used for each couple of mechanism / equivalence ratio are given in Tab.3. Since neither pyrene nor soot could be measured in Flame1.60, α_{HACA} was kept at the same value as the one of Flame1.75 for the simulations. α_{HACA} has been set to 0.02 for all simulations using the POLIMI mechanism. This value is lower than any other used to the knowledge of the authors and has been picked arbitrarily to prevent setting $\alpha_{HACA} = 0$ (i.e. not taking surface growth into account). However, even with this low value of α_{HACA}, the soot volume fraction (SVF) is significantly overestimated in Flame1.75 and Flame1.95 simulations with the POLIMI mechanism. This result is consistent with the overestimated pyrene mole fraction predicted by this mechanism as shown in Fig. 7. The other value used for α_{HACA} are within the usual range of value for this modeling parameter.

Case	Flame1.75			Flame1.95		
	U.Lille	KAUST	POLIMI	U.Lille	KAUST	POLIMI
α_{HACA}	0.175	0.25	0.02	0.4	0.35	0.02

Table. 3: Values of α_{HACA} used in each simulation

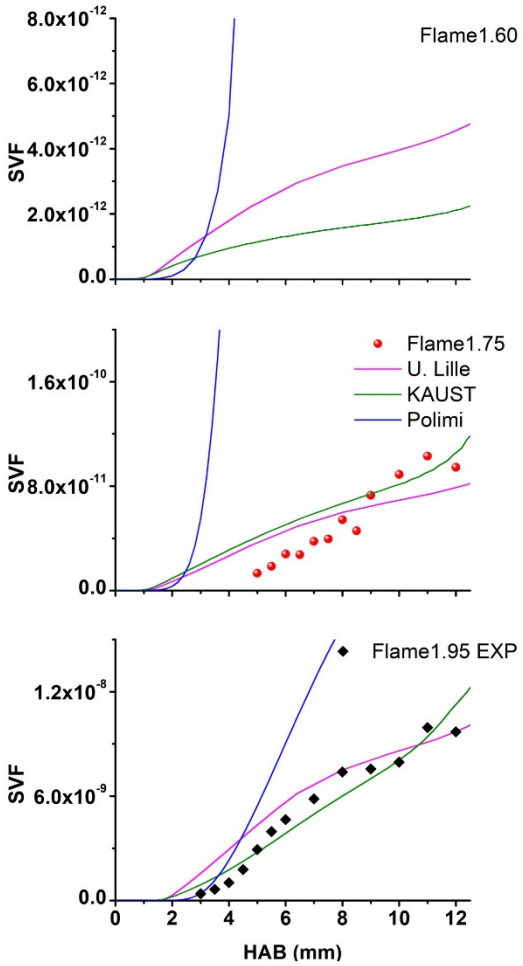

Figure 8 Flame1.60 (top), Flame1.75 (middle) and Flame1.95 (bottom): measured and modeled SVF profiles, using U.Lille (pink), KAUST (green) and POLIMI (blue) mechanisms.

SVF profiles predicted with each mechanism coupled to the soot model are given for the three flames in Fig. 8 and compared with the experimental ones. Even if a value of α_{HACA} could be found to adjust the SVF predicted by the model to the experiment for each case, the predicted SVF profiles are significantly ahead of the measured ones for Flame1.75 with a spatial shift of 2.5 mm in every simulation between the HAB at which the lowest SVF could be measured and the HAB at which the model predicts the same SVF. Concerning Flame1.95, this shift is smaller, approximately 1 mm for U.Lille and KAUST mechanisms while the simulation using POLIMI mechanism matches well with the first measurements. The discrepancy is attributed to the oversimplified particle inception model, with pyrene dimerization occurring earlier and faster than the actual processes assumed to form the first particles. For both flame conditions, even with the lowest possible effect of surface growth, SVF is significantly overestimated when the soot model is coupled to POLIMI mechanism, as mentioned above. However, α_{HACA} fitting was sufficient for the model results to agree with the experimental observation when the soot model was coupled to U.Lille and KAUST mechanism, with an error smaller than 25% between 5 mm and 12 mm HAB.

Concerning Flame1.60, this flame was considered as non-sooting since its soot yield, if any, was too low to be measured, which was expected regarding its equivalence ratio. Therefore, the model results when coupled to U.Lille or KAUST mechanisms are satisfactory with a SVF whose highest value in the burnt gases is approximatively three times smaller than the smallest SVF that could be measured experimentally (first measured point of Flame1.75).

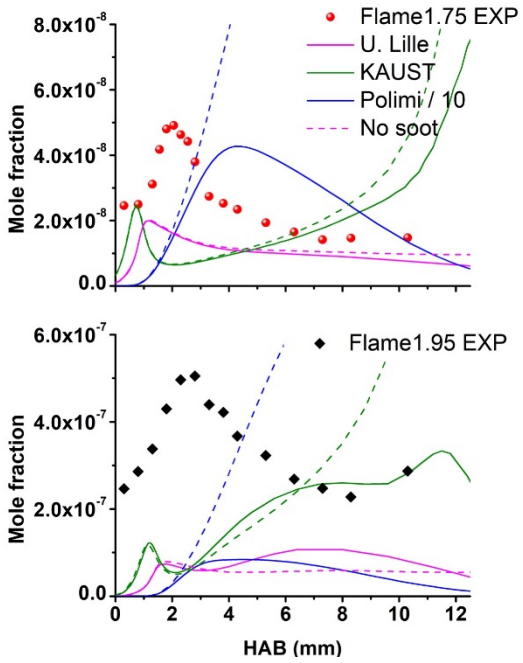

Figure 9: Flame1.75 (top) and Flame1.95 (bottom): measured (symbols) and modeled (lines) pyrene profiles. The dashed and continuous lines represent the predictions obtained respectively without and with coupling of the soot model to the gas phase mechanism.

Furthermore, all possible behaviors of the PAH adsorption/desorption (reversible condensation) model are illustrated in Fig.9. The first possibility is that profiles simulated with and without soot model can be very similar as in Flame1.75 simulations when the model is coupled with U.Lille and KAUST mechanisms because the soot yield is too small to make the consumption or formation from condensation significant. The second one is observed in both flames simulations with the POLIMI mechanism: the predicted pyrene mole fraction is significantly reduced when the POLIMI mechanism is used with the soot model because the initial predictions of pyrene (predicted by the POLIMI mechanism when not coupled to soot model) are so large that the equilibrium mainly tends to produce soot from pyrene. This behavior is reinforced by the fact that surface growth is forced to a minimal value with $\alpha_{HACA} = 0.02$ in simulations using POLIMI mechanism, generating most soot mass from pyrene

consumption. Finally, the third case is the one observed between 4 and 12 mm HAB when using U.Lille mechanism for the simulation of Flame1.95 where the pyrene mole fraction is actually increased when the soot model is switched on. This behavior is expected since surface growth is made more important in this case so the soot yield can be higher than its adsorption/desorption equilibrium value, due to surface growth action, so that desorption will be favored by the model and therefore will consume soot to form pyrene.

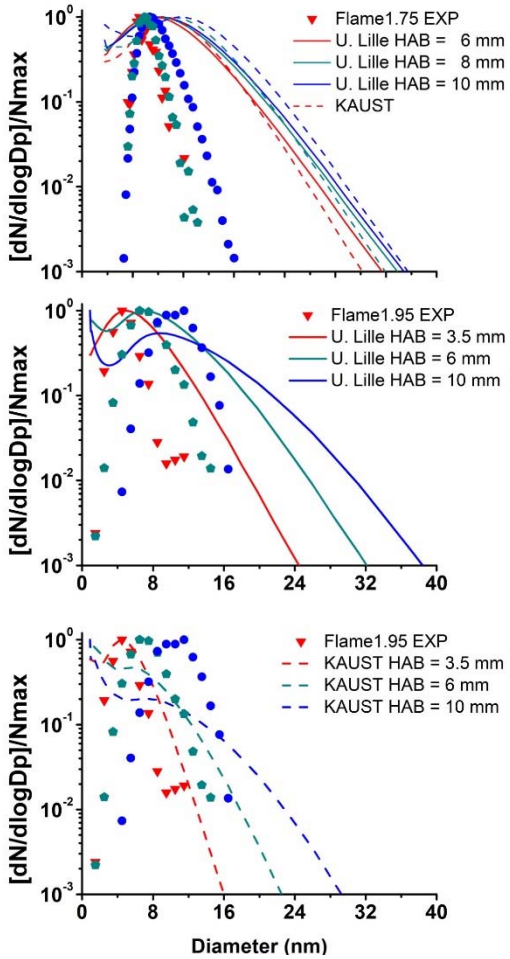

Figure 10: Primary particle diameters (symbols) measured 1nm-SMPS in Flame1.75 and by HIM in Flame1.95 and modeled particle sphere equivalent diameters distributions using U.Lille (solid lines) and KAUST (dashed lines) mechanisms. The colors represent the different HAB with 3.5mm HAB (red), 6mm HAB (green) and 10mm HAB (blue).

This analysis is completed with the comparison of the measured and predicted particle size distributions given in Fig. 10. This type of comparison cannot be used to accurately evaluate the quality of the simulations because of the differences between the definitions of the diameter in the simulations (equivalent diameter of a sphere having the same volume as the one represented by each section) and the measurements (electric mobility diameter for SMPS or primary particle diameter by HIM). Moreover, many effects influence the distributions predicted by the model such as the large uncertainties remaining on coagulation, known numerical artifact of sectional method [110] concerning diffusion in size, the effect of the way oxidation and desorption of the smallest (i.e section 1) particles are described numerically and also modelling parameters such as α_{HACA}. For instance, using a lower value for α_{HACA} would make the predicted distributions much narrower. However, this would be at the cost of the SVF predictions which would become significantly lower than expected regarding the experimental results. This inconsistency, directly due to the previously mentioned uncertainties, calls for caution for the analysis of the distributions. However, general observations can be made and the notable differences between the results measured and predicted for the two flames can safely be considered as independent of the definition of the diameter nor of these modelling uncertainties.

For instance, one of these global observations concerns the difference of three orders of magnitude shown in Fig.10 for the smallest particles predicted by the models on one side and measured on the other. This point will be discussed in the following section. The second conclusion that can be drawn from these results is that although the only fitted parameter, α_{HACA}, was fitted to reproduce the SVF, the general behavior of the main soot mode tends to be reproduced by the model. The mode peak is predicted to be at 4 nm (against 3 nm measured) in Flame1.75 at all HAB. A growth, yet harder to evaluate accurately because of the small particles overprediction, is predicted in Flame1.95 simulations as observed experimentally. The supplementary material SM4 provides the mean diameters as function of HAB, obtained experimentally and with the three mechanisms.

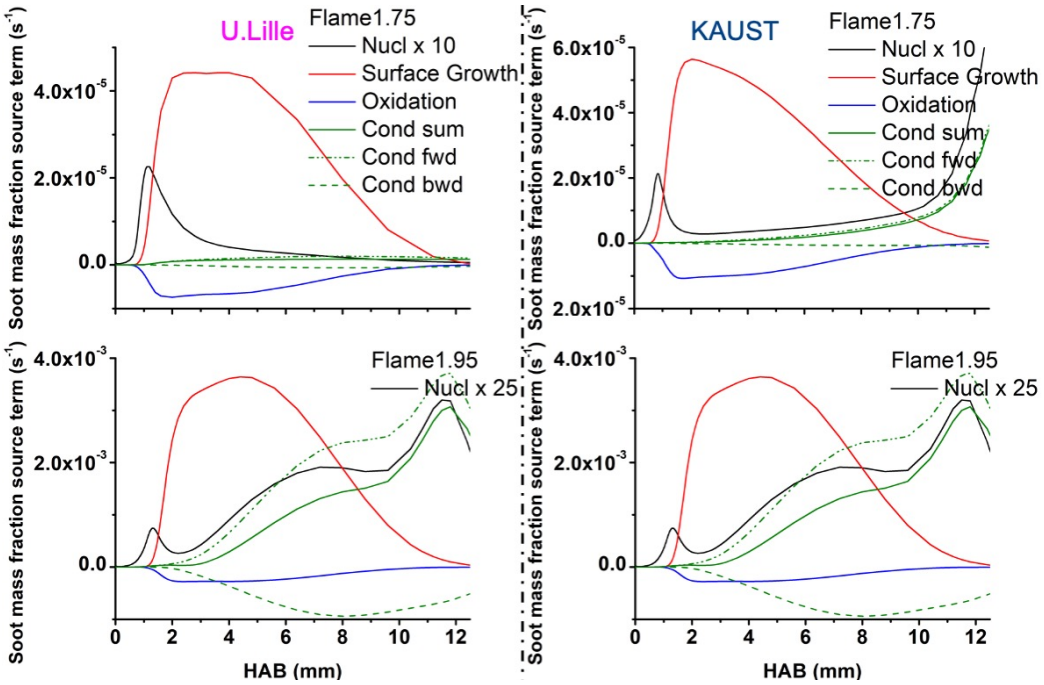

Figure 11: Flame1.75 (top) and Flame1.95 (bottom) soot mass fraction source terms profiles from simulation using KAUST mechanism. Showing nucleation (black) multiplied by 10 (top) and 100 (bottom ULille) and 25 (bottom KAUST), surface growth (red), oxidation (blue) and condensation (green) with its forward (dashed lines) and backward (mixed lines) components

Finally, the modeled soot source terms obtained with both mechanisms are given in Fig.11. Unlike the previous study on low-pressure methane flames [26,29] where the source terms of the "nucleation flame" were very different than the ones of the sooting flames, both flames show the same structure in the present case. This structure is the usual structure of sooting flames with particle inception being more than one order of magnitude lower than the dominant growth term which is the surface growth due to acetylene addition. However, particle inception is the triggering phenomenon of the whole soot formation process and the surface growth only becomes important when enough particles have been created. The difference between the two condensation profiles predicted using U.Lille or KAUST is consistent with the pyrene profile evolutions predicted with these two mechanisms. This difference shows that the influence of the PAH profile (pyrene in this case) on the predictions of the soot model is not only quantitative but also qualitative with different predicted behaviors. Measurements such as those provided in Section 2.5 will ultimately allow to prevent this issue with the validation of the gas phase. In the present case, conclusion on the expected behavior of the soot model cannot be drawn because the predictions of the two mechanisms are significantly away from the measurements.

3.3 Parametric variations and discussions: PAH-soot interactions and particle inception

The importance of introducing a phenomenon balancing PAH consumption due to PAH adsorption on soot has been shown previously for low-pressure methane/air flames [29]. This aspect is again illustrated in Flame1.95 simulations with the profiles modeled with and without such phenomenon given in Fig.12 for SVF and Fig.13 for pyrene. The SVF profiles shown in Fig.12 illustrate the effort made to minimize the error on the estimation of interactions between PAH and soot predicted by the coupling of the soot model and these two mechanisms. Indeed, these interactions are due to particle inception and condensation. Condensation depending on SVF as much as on PAH concentration, having a too large error on SVF would lead to either an overestimation or an underestimation of condensation influence on PAH profiles. To obtain these profiles, a collision efficiency has been applied to condensation in order to compensate the absence of reversibility and to fit the measured SVF profile. This efficiency is defined as in [29] with Ed = 0.05 in order to reproduce the reference (with reversibility) model SVF, thus allowing a comparison of the pyrene profiles with similar SVF. α_{HACA} has also been lowered to prevent the overestimation of the soot yield, using $\alpha_{HACA} = 0.3$ for U.Lille mechanism and $\alpha_{HACA} = 0.175$ for KAUST using only pyrene as precursor (instead of $\alpha_{HACA} = 0.4$ and $\alpha_{HACA} = 0.35$ respectively with reversibility). In Figs. 12 and 13, cases called "KAUST – all PAH" are also presented. These cases have been run using the KAUST mechanism and using all PAH larger than pyrene (of those available in the mechanism) as soot precursors for nucleation and condensation. Initially, this last simulation predicted much more soot because of the increased number of PAH implied in nucleation and condensation. Thus, α_{HACA} had to be lowered to 0.05 to match the SVF profile in order to keep comparing the influence of soot-PAH coupling with a constant amount of soot between the different cases. The resulting profiles suggest that the conclusions drawn are independent of the precursors choice because "KAUST" and "KAUST – all PAH" variation with and without reversibility are similar. Such variation could not be done with U.Lille mechanism because pyrene is one of the largest PAH considered in this model.

The pyrene profiles modeled without reversibility, with the two mechanisms, are significantly different from those obtained with reversibility and from those observed experimentally, as illustrated in Fig.13. Using the U.Lille mechanism, pyrene is consumed by soot until its value becomes more than an order of magnitude lower in the burned gases region than its peak value. This behavior is similar to the one presented in [29]. Using the KAUST mechanism, the influence of condensation reversibility is much lower with only a factor 2 between the pyrene profiles with and without reversibility. This ratio is the same whether all PAHs or only pyrene are used as precursors. The fact that the main parameter controlling PAH desorption from soot in the model had to be slightly modified between previously studied low-pressure methane flames [29] and these atmospheric butane flames illustrates the uncertainties on PAH-soot interactions. Moreover, the difference between the pyrene concentration

calculated with and without considering condensation reversibility is observed to strongly depend on the mechanism used. KAUST mechanism results highlight the possibility that with strong enough pyrene production rates, reversibility of condensation might not be as important as the results with U.Lille mechanism would suggest. A third case of flame at a higher equivalence ratio would be required to conclude about the KAUST mechanism behavior to see whether or not pyrene concentration remains at an acceptable value (within the same order of magnitude) as the measurement even when coupled with the soot model without condensation reversibility. Flame1.95 is only lightly sooting and the influence of soot on the PAH profiles is therefore not as strong as in richer flames such as the ones targeted by the International Sooting Flame (ISF) workshop [101].

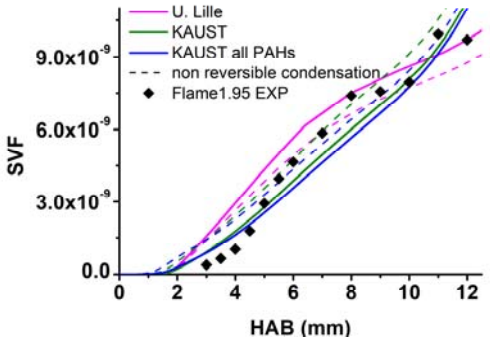

Figure 12: Flame1.95: measured (symbols) and modeled SVF profiles, including modeling without (dashed lines) and with (solid lines) condensation reversibility for U.Lille (pink) and KAUST (green) mechanisms using only pyrene as precursor and KAUST using all PAH larger than pyrene as precursors (blue). The value of α was adjusted in each case to fit the value of SVF in the burnt gases.

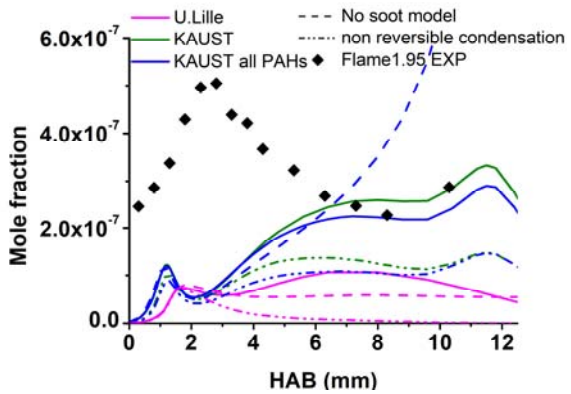

Figure 13: Flame1.95: measured (symbols) and modeled pyrene profiles, including modeling without soot model (dashed lines) and with soot model including cases without (mixed lines) and with (solid

lines) condensation reversibility for U.Lille (pink) and KAUST (green) mechanisms using only pyrene as precursor and KAUST using all PAH larger than pyrene as precursors (blue).

Finally, particle size distributions of Flame1.95 with and without reversibility are plotted for U.Lille and KAUST mechanism (using only pyrene as precursor) in Fig.14. Experimental measurements have been withdrawn from these plots for the sake of clarity (they are given in Fig 10). Again, the behaviors differ for the two mechanisms. Coupling the U.Lille mechanism with the soot model without condensation reversibility leads to a predicted distribution showing a single mode growing with the distance from burner since there is no more pyrene to generate small particles, as previously observed in [29]. By contrast, the distributions predicted without reversibility when using the KAUST mechanism are different with a first peak of very small particles (around 1nm) remaining even at the furthest plotted HAB. Using the KAUST mechanism, even without taking into account condensation reversibility, enough pyrene is still predicted so that very small particles directly due to nucleation are still produced. These comparisons highlight again the fact that not only quantitative but also qualitative differences can be due to the choice of the gas phase mechanism for soot modelling. It also pleads for more work on the nucleation process. Indeed, whether it is due to condensation reversibility or not, the presence of PAHs currently leads to a peak of very small particles which is not observed with the used techniques in this work. Although there are several sources of uncertainties in the predicted distributions, the major difference between a growing mode and what is predicted in the three cases where pyrene is not negligible in the burned gases region (most particles being of the smallest size) make this conclusion about particle inception safe to believe. This means that the nucleation model lack of a controlling factor in order to reduce the formation of particles in the burned gases region. Hence, the interest of these flames to validate more advanced and future nucleation models [4,9] to be developed, appears clearly from these observations. This conclusion is local to the burned gases region where soot and PAH should be both present in non-negligible quantities and does not mean the overall (integrate on all the domain) nucleation rate is overestimated.

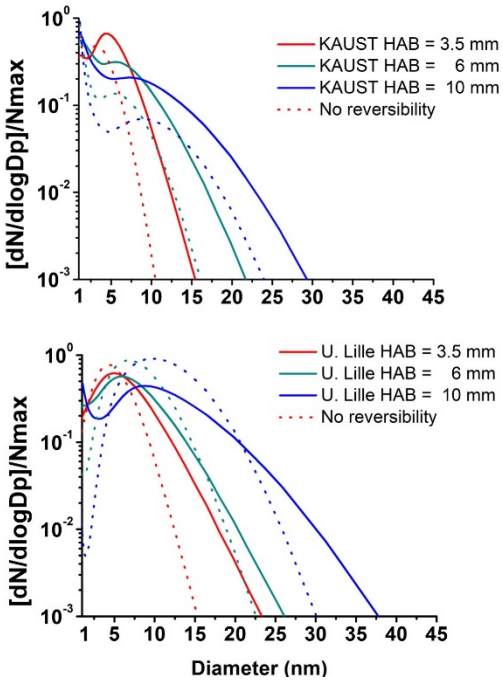

Figure 14: Flame1.95 modeled normalized particle size distributions at several HAB with (solid lines) and without (dashed lines) condensation reversibility for U.Lille (top) and KAUST (bottom) mechanisms

.

4 Conclusion

In this work, we investigated the chemical structure of three premixed n-butane/O_2/N_2 flames offering the possibility of exploring the transition from a soot-free condition at phi=1.6 to a lightly sooting condition at phi=1.95. The intermediate flame at phi=1.75 is a nucleation flame. In this kind of flame, the soot particles, formed a few mm above the burner surface, keep a very small size (2-4 nm) throughout the HAB, indicating negligible growth with residence time. This unique specificity is very interesting for understanding the early steps of soot formation.

The soot volume fraction ranges from 0.1 ppb in the burnt gases of Flame1.75 to 10 ppb in Flame1.95. In this latter flame, the diameters of the primary soot particles exceed 10 nm. The soot volume fraction obtained by laser induced incandescence and the size distributions obtained by helium ion microscopy and by scanning mobility particle sizing were previously published in [31] and [27]. However, the initial size distributions obtained by SMPS [27] were corrected here to account for the transition from diffuse to specular scattering, and the van der Waals gas–particle interactions. The soot database is enriched in this work thanks to the mole fraction profiles of many stable species measured by gas chromatography and by Jet-cooled Laser induced fluorescence for the PAHs. Among them, several species exhibit high sensitivity, reaching more than a decade over the range of equivalence ratios, particularly acetylene,

propyne, 1-butyne, benzene, naphthalene and pyrene species. This constitutes a valuable database for soot modeling.

In order to explore these experimental observations, the chemical flame structure of these flames was modeled using three kinetic mechanisms from the literature, referred as U.Lille, KAUST and POLIMI, to which a recently developed soot model [29], based on a sectional approach, was coupled. Overall, the KAUST mechanism gives the most satisfactory results on a wide range of gaseous species involved in the PAH and soot formation.

The modeling of soot in these flames highlighted the interest of such cases concerning both the choice of the conditions and the measurements performed. While the global quantities describing soot such as the SVF and mean diameters could be reproduced with minimal model adjustment, the modeling of the particles distributions showed significant differences with the experimental observations. Having combined measurements of SVF, size distributions and PAH provides references to analyze results and variations (parameters and mechanisms). This allows new conclusions to be drawn and justified regarding the soot model behavior and some global aspects of soot modeling.

First, the influence of the gas-phase mechanism turned out to be significant not only quantitatively but also qualitatively with very different soot formation process favored by the same soot model depending on the mechanism it was coupled with. Some conclusions from a previous study, such as the need of taking into account condensation reversibility to predict PAH in accordance with measurements are mechanism dependent. The exhaustive database provided in Section 2.5 will help sorting this issue out by allowing extended gas-phase mechanisms validations. Second, these cases allowed to point out that one cannot predict particles distributions with a simple collision-based particle inception model. This result was expected based on molecular modeling studies of the last decade on this topic [3,89,92] but larger scale model using this assumption could not be questioned so far mostly because of the scarcity of PAH measurements.

Acknowledgments

The project (ASMAPE) was funded by the French National Research Agency (ANR) under contract ANR-13-TDMO-0002. This work is a contribution to the LabEx CaPPA project funded by ANR under contract ANR-11-LABX-0005-01 and to the CPER research project CLIMIBIO funded by the French Ministère de l'Enseignement Supérieur et de la Recherche. The authors thank the Regional Council «Hauts-de-France » and the « European Regional Development Fund » for their financial support to these projects". The authors thank O. Hombert for his mechanical assistance and S. Gosselin for her assistance in GC measurements.

References :

[1] C.A. Schuetz, M. Frenklach , Nucleation of soot: Molecular dynamics simulations of pyrene dimerization, Proc. Combust. Inst. 29(2) (2002) 2307–14.
[2] M. Frenklach , Reaction mechanism of soot formation in flames, Phys. Chem. Chem. Phys. 4(11) (2002) 2028–37.
[3] K.O. Johansson, T. Dillstrom, P. Elvati, M.F. Campbell, P.E. Schrader, D.M. Popolan-Vaida, N.K. Richards-Henderson, K.R. Wilson, A. Violi, H.A. Michelsen , Radical–radical reactions, pyrene nucleation, and incipient soot formation in combustion, Proc. Combust. Inst. 36(1) (2017) 799–806.
[4] M.R. Kholghy, G.A. Kelesidis, S.E. Pratsinis , Reactive polycyclic aromatic hydrocarbon dimerization drives soot nucleation, Phys. Chem. Chem. Phys. 20(16) (2018) 10926–38.
[5] K.O. Johansson, M.P. Head-Gordon, P.E. Schrader, K.R. Wilson, H.A. Michelsen , Resonance-stabilized hydrocarbon-radical chain reactions may explain soot inception and growth, Science 361(6406) (2018) 997–1000.
[6] X. Mercier, O. Carrivain, C. Irimiea, A. Faccinetto, E. Therssen , Dimers of polycyclic aromatic hydrocarbons: the missing pieces in the soot formation process, Phys. Chem. Chem. Phys. 21(16) (2019) 8282–94.
[7] A. Faccinetto, C. Irimiea, P. Minutolo, M. Commodo, A. D'Anna, N. Nuns, Y. Carpentier, C. Pirim, P. Desgroux, C. Focsa, X. Mercier , Evidence on the formation of dimers of polycyclic aromatic hydrocarbons in a laminar diffusion flame, Commun. Chem. 3(1) (2020) 1–8.
[8] H. Wang , Formation of nascent soot and other condensed-phase materials in flames, Proc. Combust. Inst. 33(1) (2011) 41–67.
[9] M. Frenklach, A.M. Mebel , On the mechanism of soot nucleation, Phys. Chem. Chem. Phys. 22(9) (2020) 5314–31.
[10] T.R. Melton, F. Inal, S.M. Senkan , The effects of equivalence ratio on the formation of polycyclic aromatic hydrocarbons and soot in premixed ethane flames, Combust. Flame 121(4) (2000) 671–8.
[11] F. Xu, P.B. Sunderland, G.M. Faeth , Soot formation in laminar premixed ethylene/air flames at atmospheric pressure, Combust. Flame 108(4) (1997) 471–93.
[12] N.M. Marinov, W.J. Pitz, C.K. Westbrook, A.M. Vincitore, M.J. Castaldi, S.M. Senkan, C.F. Melius , Aromatic and polycyclic aromatic hydrocarbon formation in a laminar premixed n-butane flame, Combust. Flame 114(1) (1998) 192–213.
[13] J. Camacho, S. Lieb, H. Wang , Evolution of size distribution of nascent soot in n- and i-butanol flames, Proc. Combust. Inst. 34(1) (2013) 1853–60.
[14] A. D'Anna, A. Ciajolo, M. Alfè, B. Apicella, A. Tregrossi , Effect of fuel/air ratio and aromaticity on the molecular weight distribution of soot in premixed n-heptane flames, Proc. Combust. Inst. 32(1) (2009) 803–10.
[15] M.J. Castaldi, S.M. Senkan , PAH Formation in the Premixed Flame of Ethane, Combust. Sci. Technol. 116–117(1–6) (1996) 167–81.
[16] A. El Bakali, J.-L. Delfau, C. Vovelle, Experimental Study of 1 Atmosphere, Rich, Premixed n-heptane and iso-octane Flames, Combust. Sci. Technol. 140(1–6) (1998) 69–91.
[17] A. El Bakali, J.L. Delfau, R. Akrich, C. Vovelle , Measurement of soot volume fraction and gaseous species concentrations in premixed N-heptane and iso-octane flames, J. Chim. Phys. 94 (1997) 1659–73.
[18] A. El Bakali, J.-L. Delfau, C. Vovelle , Kinetic modeling of a rich, atmospheric pressure, premixed n-heptane/O2/N2 flame, Combust. Flame 118(3) (1999) 381–98.
[19] M. Frenklach, H. Wang , Detailed modeling of soot particle nucleation and growth, Symp. Int. Combust. 23(1) (1991) 1559–66.
[20] A.B. Fialkov, K.-H. Homann , Large molecules, ions, radicals, and small soot particles in fuel-rich hydrocarbon flames: Part VI: positive ions of aliphatic and aromatic hydrocarbons in a low-pressure premixed flame of n-butane and oxygen1 1Part I, ref. 7; part II, ref. 8; part III, ref. 4; Part IV, ref. 5; part V, ref. 6., Combust. Flame 127(3) (2001) 2076–90.
[21] M. Salamanca, J. Wullenkord, I. Graf, S. Schmitt, L. Ruwe, K. Kohse-Höinghaus , An experimental laminar flame investigation of dual-fuel mixtures of C4 methyl esters with C2–C4 hydrocarbon base fuels, Proc. Combust. Inst. 37(2) (2019) 1725–32.
[22] A.M. Valencia-López, F. Bustamante, A. Loukou, B. Stelzner, D. Trimis, M. Frenklach, N.A. Slavinskaya , Effect of benzene doping on soot precursors formation in non-premixed flames of

producer gas (PG), Combust. Flame 207 (2019) 265–80.
[23] C.S. McEnally, L.D. Pfefferle, B. Atakan, K. Kohse-Höinghaus , Studies of aromatic hydrocarbon formation mechanisms in flames: Progress towards closing the fuel gap, Prog. Energy Combust. Sci. 32(3) (2006) 247–94.
[24] T. Mouton, X. Mercier, M. Wartel, N. Lamoureux, P. Desgroux , Laser-induced incandescence technique to identify soot nucleation and very small particles in low-pressure methane flames, Appl. Phys. B 112(3) (2013) 369–79.
[25] H. Bladh, N.-E. Olofsson, T. Mouton, J. Simonsson, X. Mercier, A. Faccinetto, P.-E. Bengtsson, P. Desgroux , Probing the smallest soot particles in low-sooting premixed flames using laser-induced incandescence, Proc. Combust. Inst. 35(2) (2015) 1843–50.
[26] P. Desgroux, A. Faccinetto, X. Mercier, T. Mouton, D. Aubagnac Karkar, A. El Bakali , Comparative study of the soot formation process in a “nucleation” and a “sooting” low pressure premixed methane flame, Combust. Flame 184 (2017) 153–66.
[27] C. Betrancourt, F. Liu, P. Desgroux, X. Mercier, A. Faccinetto, M. Salamanca, L. Ruwe, K. Kohse-Höinghaus, D. Emmrich, A. Beyer, A. Gölzhäuser, T. Tritscher , Investigation of the size of the incandescent incipient soot particles in premixed sooting and nucleation flames of *n* -butane using LII, HIM, and 1 nm-SMPS, Aerosol Sci. Technol. 51(8) (2017) 1–20.
[28] H.-Q. Do, L.-S. Tran, L. Gasnot, X. Mercier, A. El Bakali , Experimental study of the influence of hydrogen as a fuel additive on the formation of soot precursors and particles in atmospheric laminar premixed flames of methane, Fuel 287 (2021) 119517.
[29] D. Aubagnac-Karkar, A. El Bakali, P. Desgroux , Soot particles inception and PAH condensation modelling applied in a soot model utilizing a sectional method, Combust. Flame 189 (2018) 190–206.
[30] T. Mitra, T. Zhang, A.D. Sediako, M.J. Thomson , Understanding the formation and growth of polycyclic aromatic hydrocarbons (PAHs) and young soot from n-dodecane in a sooting laminar coflow diffusion flame, Combust. Flame 202 (2019) 33–42.
[31] C. Betrancourt, X. Mercier, F. Liu, P. Desgroux, Quantitative measurement of volume fraction profiles of soot of different maturities in premixed flames by extinction-calibrated laser-induced incandescence, Appl. Phys. B 125(1) (2019) 16.
[32] Y. Huang, C.J. Sung, J.A. Eng, Dilution limits of n-butane/air mixtures under conditions relevant to HCCI combustion, Combust. Flame 136(4) (2004) 457–66.
[33] P. Oßwald, K. Kohse-Höinghaus, U. Struckmeier, T. Zeuch, L. Seidel, L. Leon, F. Mauss, Combustion Chemistry of the Butane Isomers in Premixed Low-Pressure Flames, Z. Für Phys. Chem. 225(9–10) (2011) 1029–54.
[34] W.J. Pitz, C.K. Westbrook, Chemical kinetics of the high pressure oxidation of n-butane and its relation to engine knock, Combust. Flame 63(1) (1986) 113–33.
[35] W.J. Pitz, C.K. Westbrook, W.R. Leppard, Autoignition chemistry of n-butane in a motored engine: A comparison of experimental and modeling results, SAE Technical Paper, 1988.
[36] J.C. Prince, C. Treviño, F.A. Williams, A reduced reaction mechanism for the combustion of n-butane, Combust. Flame 175 (2017) 27–33.
[37] P. Rodrigues, B. Franzelli, R. Vicquelin, O. Gicquel, N. Darabiha, Coupling an LES approach and a soot sectional model for the study of sooting turbulent non-premixed flames, Combust. Flame 190 (2018) 477-499.
[38] T. Blacha, M. Di Domenico, P. Gerlinger, M. Aigner, Soot predictions in premixed and non-premixed laminar flames using a sectional approach for PAHs and soot, Combust. Flame 159 (2012) 181-193.
[39] M.E.Mueller, G.Blanquart, H.Pitsch, Hybrid Method of Moments for modeling soot formation and growth, Combust. Flame 156 (2009) 1143-1155.
[40] W. Pejpichestakul, E. Ranzi, M. Pelucchi, A. Frassoldati, A. Cuoci, A. Parente, T. Faravelli, Examination of a soot model in premixed laminar flames at fuel-rich conditions, Proc. Combust. Inst. 37(1) (2019) 1013-1021,
[41] A. Khanehzar, F. Cepeda, S. B.Dworkin, The influence of nitrogen and hydrogen addition/dilution on soot formation in coflow ethylene/air diffusion flames, Fuel 309 (2022) 122244.

[42] A. Mansouri, L. Zimmer, S. B. Dworkin, N. A. Eaves, Impact of pressure-based HACA rates on soot formation in varying-pressure coflow laminar diffusion flames, Combust. Flame 218 (2020) 109-120.
[43] C. Saggese, A. Cuoci, A. Frassoldati, S. Ferrario, J. Camacho, H. Wang, T. Faravelli , Probe effects in soot sampling from a burner-stabilized stagnation flame, Combust. Flame 167 (2016) 184–97.
[44] A. El Bakali, D. Boufflers, C. Betrancourt, P. Desgroux , Experimental and numerical investigation of atmospheric laminar premixed n-butane flames in sooting conditions, Fuel 211 (2018) 548–65.
[45] A. Denisov, G. Colmegna, P. Jansohn , Temperature measurements in sooting counterflow diffusion flames using laser-induced fluorescence of flame-produced nitric oxide, Appl. Phys. B 116(2) (2014) 339–46.
[46] J. Luque, D.R. Crosley , LIFBASE (version 1.5), SRI Int. Rep. MP (1999) 99–009.
[
[47] X. Mercier, M. Wartel, J.-F. Pauwels, P. Desgroux , Implementation of a new spectroscopic method to quantify aromatic species involved in the formation of soot particles in flames, Appl. Phys. B 91(2) (2008) 387–95.
[48] M. Wartel, J.-F. Pauwels, P. Desgroux, X. Mercier , Quantitative measurement of naphthalene in low-pressure flames by jet-cooled laser-induced fluorescence, Appl. Phys. B 100(4) (2010) 933–43.
[49] M. Wartel, J.-F. Pauwels, P. Desgroux, X. Mercier , Pyrene Measurements in Sooting Low Pressure Methane Flames by Jet-Cooled Laser-Induced Fluorescence, J. Phys. Chem. A 115(49) (2011) 14153–62.
[50] T. Mouton, X. Mercier, P. Desgroux , Isomer discrimination of PAHs formed in sooting flames by jet-cooled laser-induced fluorescence: application to the measurement of pyrene and fluoranthene, Appl. Phys. B 122(5) (2016) 123.
[51] L.A. Sgro, A.C. Barone, M. Commodo, A. D'Alessio, A. De Filippo, G. Lanzuolo, P. Minutolo, Measurement of nanoparticles of organic carbon in non-sooting flame conditions, Proc. Combust. Inst. 32(1) (2009) 689–96.
[52] M. Kazemimanesh, A. Moallemi, J.S. Olfert, L.W. Kostiuk , Probe sampling to map and characterize nanoparticles along the axis of a laminar methane jet diffusion flame, Proc. Combust. Inst. 36(1) (2017) 881–8.
[53] A.D. Abid, E.D. Tolmachoff, D.J. Phares, H. Wang, Y. Liu, A. Laskin , Size distribution and morphology of nascent soot in premixed ethylene flames with and without benzene doping, Proc. Combust. Inst. 32(1) (2009) 681–8.
[54] B. Zhao, Z. Yang, Z. Li, M.V. Johnston, H. Wang , Particle size distribution function of incipient soot in laminar premixed ethylene flames: effect of flame temperature, Proc. Combust. Inst. 30(1) (2005) 1441–8.
[55] Z. Li, H. Wang , Drag force, diffusion coefficient, and electric mobility of small particles. I. Theory applicable to the free-molecule regime, Phys. Rev. E 68(6) (2003).
[56] Z. Li, H. Wang , Drag force, diffusion coefficient, and electric mobility of small particles. II. Application, Phys. Rev. E Stat. Nonlin. Soft Matter Phys. 68(6 Pt 1) (2003) 061207.
[57] C. Gu, H. Lin, J. Camacho, B. Lin, C. Shao, R. Li, H. Gu, B. Guan, Z. Huang, H. Wang , Particle size distribution of nascent soot in lightly and heavily sooting premixed ethylene flames, Combust. Flame 165 (2016) 177–87.
[58] A.D. Abid, N. Heinz, E.D. Tolmachoff, D.J. Phares, C.S. Campbell, H. Wang , On evolution of particle size distribution functions of incipient soot in premixed ethylene–oxygen–argon flames, Combust. Flame 154(4) (2008) 775–88.
[59] C.A. Echavarria, A.F. Sarofim, J.S. Lighty, A. D'Anna , Evolution of soot size distribution in premixed ethylene/air and ethylene/benzene/air flames: Experimental and modeling study, Combust. Flame 158(1) (2011) 98–104.
[60] Z. Li, H. Wang , Thermophoretic force and velocity of nanoparticles in the free molecule regime, Phys. Rev. E 70(2) (2004).
[61] N.M. Marinov, W.J. Pitz, C.K. Westbrook, A.M. Vincitore, M.J. Castaldi, S.M. Senkan, C.F. Melius , Aromatic and Polycyclic Aromatic Hydrocarbon Formation in a Laminar Premixed n-Butane Flame, Combust. Flame 114(1) (1998) 192–213.
[62] J.D. Bittner, J.B. Howard , Composition profiles and reaction mechanisms in a near-sooting

premixed benzene/oxygen/argon flame, Symp. Int. Combust. 18(1) (1981) 1105–16.
[63] F. Inal, S.M. Senkan , Effects of equivalence ratio on species and soot concentrations in premixed n-heptane flames, Combust. Flame 131(1) (2002) 16–28.
[64] F. Defoeux, V. Dias, C. Renard, P.J. Van Tiggelen, J. Vandooren , Experimental investigation of the structure of a sooting premixed benzene/oxygen/argon flame burning at low pressure, Proc. Combust. Inst. 30(1) (2005) 1407–15.
[65] V. Dias, H.M. Katshiatshia, H. Jeanmart , The influence of ethanol addition on a rich premixed benzene flame at low pressure, Combust. Flame 161(9) (2014) 2297–304.
[66] H. Jin, A. Frassoldati, Y. Wang, X. Zhang, M. Zeng, Y. Li, F. Qi, A. Cuoci, T. Faravelli , Kinetic modeling study of benzene and PAH formation in laminar methane flames, Combust. Flame 162(5) (2015) 1692–711.
[67] Y. Li, L. Zhang, Z. Tian, T. Yuan, K. Zhang, B. Yang, F. Qi , Investigation of the rich premixed laminar acetylene/oxygen/argon flame: Comprehensive flame structure and special concerns of polyynes, Proc. Combust. Inst. 32(1) (2009) 1293–300.
[68] A. Mze Ahmed, S. Mancarella, P. Desgroux, L. Gasnot, J.-F. Pauwels, A. El Bakali , Experimental and numerical study on rich methane/hydrogen/air laminar premixed flames at atmospheric pressure: Effect of hydrogen addition to fuel on soot gaseous precursors, Int. J. Hydrog. Energy 41(16) (2016) 6929–42.
[69] J. Yang, L. Zhao, W. Yuan, F. Qi, Y. Li , Experimental and kinetic modeling investigation on laminar premixed benzene flames with various equivalence ratios, Proc. Combust. Inst. 35(1) (2015) 855–62.
[70] J.A. Cole, J.D. Bittner, J.P. Longwell, J.B. Howard , Formation mechanisms of aromatic compounds in aliphatic flames, Combust. Flame 56(1) (1984) 51–70.
[71] J.A. Miller, C.F. Melius , Kinetic and thermodynamic issues in the formation of aromatic compounds in flames of aliphatic fuels, Combust. Flame 91(1) (1992) 21–39.
[72] C.F. Melius, M.E. Colvin, N.M. Marinov, W.J. Pit, S.M. Senkan , Reaction mechanisms in aromatic hydrocarbon formation involving the C5H5 cyclopentadienyl moiety, Symp. Int. Combust. 26(1) (1996) 685–92.
[73] M. Frenklach, J. Warnatz , Detailed Modeling of PAH Profiles in a Sooting Low-Pressure Acetylene Flame, Combust. Sci. Technol. 51(4–6) (1987) 265–83.
[74] H.A. Michelsen, M.B. Colket, P.-E. Bengtsson, A. D'Anna, P. Desgroux, B.S. Haynes, J.H. Miller, G.J. Nathan, H. Pitsch, H. Wang , A Review of Terminology Used to Describe Soot Formation and Evolution under Combustion and Pyrolytic Conditions, ACS Nano 14(10) (2020) 12470–90.
[75] D. Aubagnac-Karkar, J.-B. Michel, O. Colin, P.E. Vervisch-Kljakic, N. Darabiha , Sectional soot model coupled to tabulated chemistry for Diesel RANS simulations, Combust. Flame 162(8) (2015) 3081–99.
[76] D.G. Goodwin, R.L. Speth, H.K. Moffat, B.W. Weber Cantera: An Object-oriented Software Toolkit for Chemical Kinetics, Thermodynamics, and Transport Processes, Zenodo, 2018.
[77] A. El Bakali, X. Mercier, M. Wartel, F. Acevedo, I. Burns, L. Gasnot, J.-F. Pauwels, P. Desgroux , Modeling of PAHs in low pressure sooting premixed methane flame, Energy 43(1) (2012) 73–84.
[78] S. Park, Y. Wang, S.H. Chung, S.M. Sarathy , Compositional effects on PAH and soot formation in counterflow diffusion flames of gasoline surrogate fuels, Combust. Flame 178 (2017) 46–60.
[79] E. Ranzi, A. Frassoldati, S. Granata, T. Faravelli , Wide-Range Kinetic Modeling Study of the Pyrolysis, Partial Oxidation, and Combustion of Heavy n-Alkanes, Ind. Eng. Chem. Res. 44(14) (2005) 5170–83.
[80] M.R. Djokic, K.M. Van Geem, C. Cavallotti, A. Frassoldati, E. Ranzi, G.B. Marin , An experimental and kinetic modeling study of cyclopentadiene pyrolysis: First growth of polycyclic aromatic hydrocarbons, Combust. Flame 161(11) (2014) 2739–51.
[81] T. Bieleveld, A. Frassoldati, A. Cuoci, T. Faravelli, E. Ranzi, U. Niemann, K. Seshadri , Experimental and kinetic modeling study of combustion of gasoline, its surrogates and components in laminar non-premixed flows, Proc. Combust. Inst. 32(1) (2009) 493–500.
[82] C. Saggese, A. Frassoldati, A. Cuoci, T. Faravelli, E. Ranzi , A wide range kinetic modeling study of pyrolysis and oxidation of benzene, Combust. Flame 160(7) (2013) 1168–90.
[83] S. Bejaoui, S. Batut, E. Therssen, N. Lamoureux, P. Desgroux, F. Liu , Measurements and

modeling of laser-induced incandescence of soot at different heights in a flat premixed flame, Appl. Phys. B 118(3) (2015) 449–69.
[84] U. Struckmeier, P. Oßwald, T. Kasper, L. Böhling, M. Heusing, M. Köhler, A. Brockhinke, K. Kohse-Höinghaus , Sampling Probe Influences on Temperature and Species Concentrations in Molecular Beam Mass Spectroscopic Investigations of Flat Premixed Low-pressure Flames, Z. Für Phys. Chem. 223(4–5) (2009) 503–37.
[85] P.A. Skovorodko, A.G. Tereshchenko, O.P. Korobeinichev, D.A. Knyazkov, A.G. Shmakov , Experimental and numerical study of probe-induced perturbations of the flame structure, Combust. Theory Model. 17(1) (2013) 1–24.
[86] N. Lamoureux, P. Desgroux , In Situ Laser-Induced Fluorescence and Ex Situ Cavity Ring-Down Spectroscopy Applied to NO Measurement in Flames: Microprobe Perturbation and Absolute Quantification, Energy Fuels (2021).
[87] J. Appel, H. Bockhorn, M. Frenklach , Kinetic modeling of soot formation with detailed chemistry and physics: laminar premixed flames of C2 hydrocarbons, Combust. Flame 121(1) (2000) 122–36.
[88] M. v. Smoluchowski , Versuch einer mathematischen Theorie der Koagulationskinetik kolloider Lösungen, Z. Für Phys. Chem. 92U(1) (1918) 129–68.
[89] P. Elvati, A. Violi , Thermodynamics of poly-aromatic hydrocarbon clustering and the effects of substituted aliphatic chains, Proc. Combust. Inst. 34(1) (2013) 1837–43.
[90] J.Y.W. Lai, P. Elvati, A. Violi , Stochastic atomistic simulation of polycyclic aromatic hydrocarbon growth in combustion, Phys. Chem. Chem. Phys. 16(17) (2014) 7969–79.
[91] J.S. Lowe, J.Y.W. Lai, P. Elvati, A. Violi , Towards a predictive model for polycyclic aromatic hydrocarbon dimerization propensity, Proc. Combust. Inst. 35(2) (2015) 1827–32.
[92] H. Sabbah, L. Biennier, S.J. Klippenstein, I.R. Sims, B.R. Rowe , Exploring the Role of PAHs in the Formation of Soot: Pyrene Dimerization, J. Phys. Chem. Lett. 1(19) (2010) 2962–7.
[93] B.A. Adamson, S.A. Skeen, M. Ahmed, N. Hansen, Nucleation of soot: experimental assessment of the role of polycyclic aromatic hydrocarbon (PAH) dimers, Z. Phys. Chem. 234(7-9) (2020) 1295-1310.
[94] J. Singh, M. Balthasar, M. Kraft, W. Wagner , Stochastic modeling of soot particle size and age distributions in laminar premixed flames, Proc. Combust. Inst. 30(1) (2005) 1457–65.
[95] J. Appel, H. Bockhorn, M. Wulkow , A detailed numerical study of the evolution of soot particle size distributions in laminar premixed flames, Chemosphere 42(5) (2001) 635–45.
[96] J.S. Bhatt, R.P. Lindstedt , Analysis of the impact of agglomeration and surface chemistry models on soot formation and oxidation, Proc. Combust. Inst. 32(1) (2009) 713–20.
[97] S. Salenbauch, A. Cuoci, A. Frassoldati, C. Saggese, T. Faravelli, C. Hasse , Modeling soot formation in premixed flames using an Extended Conditional Quadrature Method of Moments, Combust. Flame 162(6) (2015) 2529–43.
[98] R.P. Lindstedt, B.B.O. Waldheim , Modeling of soot particle size distributions in premixed stagnation flow flames, Proc. Combust. Inst. 34(1) (2013) 1861–8.
[99] R. Zacharia, H. Ulbricht, T. Hertel, Interlayer Cohesive Energy of Graphite from Thermal Desorption of Polyaromatic Hydrocarbons, Phys. Rev. B: Condens. Matter Mater. Phys. 69 (2004) 155406.
[100] Y. Bedjanian, M.L. Nguyen, A. Guilloteau, Desorption of Polycyclic Aromatic Hydrocarbons from Soot Surface: Five- and SixRing (C22, C24) PAHs, J. Phys. Chem. A 114 (2010) 3533−3539.
[101] Y. Zhou, Q. Chu, D. Hou, D. Chen, X. You, J. Phys. Chem. A 126 (2022) 630–639.
[102] T.S. Totton, A.J. Misquitta, M. Kraft , A quantitative study of the clustering of polycyclic aromatic hydrocarbons at high temperatures, Phys. Chem. Chem. Phys. 14(12) (2012) 4081–94.
[103] N.A. Eaves, S. Dworkin, M. Thomson, The importance of reversibility in modeling soot nucleation and condensation processes, Proc. Combust. Inst. 35 (2015) 1787–1794.
[104] A. Veshkini, S.B. Dworkin, M.J. Thomson , A soot particle surface reactivity model applied to a wide range of laminar ethylene/air flames, Combust. Flame 161(12) (2014) 3191–200.
[105] A. D'Anna, J.H. Kent , Modeling of particulate carbon and species formation in coflowing diffusion flames of ethylene, Combust. Flame 144(1) (2006) 249–60.
[106] A. D'Anna , Detailed Kinetic Modeling of Particulate Formation in Rich Premixed Flames of Ethylene, Energy Fuels 22(3) (2008) 1610–9.

[107] A. D'Anna, J.H. Kent , A model of particulate and species formation applied to laminar, nonpremixed flames for three aliphatic-hydrocarbon fuels, Combust. Flame 152(4) (2008) 573–87.
[108] M. Frenklach , New form for reduced modeling of soot oxidation: Accounting for multi-site kinetics and surface reactivity, Combust. Flame 201 (2019) 148–59.
[109] C. Saggese, S. Ferrario, J. Camacho, A. Cuoci, A. Frassoldati, E. Ranzi, H. Wang, T. Faravelli, Kinetic modeling of particle size distribution of soot in a premixed burner-stabilized stagnation ethylene flame, Combust. Flame 162(9) (2015) 3356–69.
[110] A. Bouaniche, L. Vervisch, P. Domingo , A hybrid stochastic/fixed-sectional method for solving the population balance equation, Chem. Eng. Sci. 209 (2019) 115198.
[111] International Sooting Flame (ISF) Workshop. https://www.adelaide.edu.au/cet/isfworkshop/

.

Figure caption

Figure 1 The normalized PSDF (raw [27] and corrected (this work)) of the diameter measured by 1 nm-SMPS at 6, 8, and 10 mm in Flame1.75. The filled and empty symbols are respectively raw and corrected data from nanoparticle transport theory [53].The lines are fits to data using a lognormal distribution function and the corresponding fitting parameters are shown in the figure.

Figure 2 Profiles of selected aliphatic compounds: acetylene, propyne and 1-butyne, measured by GC in the flames at ϕ =1.60, 1.75 and 1.95.

Figure 3 Profiles of aromatic compounds measured by GC (benzene) and JCLIF (naphthalene and pyrene) in the flames at ϕ =1.60, 1.75 and 1.95.

Figure 4 Soot volume fraction profiles f_v , HIM and 1nm-SMPS PSDFs and HIM pictures in Flame1.95 (left column) and Flame1.75 (right column) previously measured in [27,31]. Soot formation steps are schematically represented on the f_v profiles as function of HAB in each flame. The dashed lines are fits to data using a lognormal distribution function whose corresponding fitting parameters are indicated in the inset. The spatial resolution of HIM measurements due to the sampling procedure is ± 1 mm (see supplementary material SM2). That of the SMPS measurements could not be estimated.

Figure 5 Comparison between the predicted (lines) and the measured (symbols) mole fraction profiles of C_2H_2 in Flame1.60. Closed symbols represent the experimental data (open symbols) shifted by 1.7 mm towards the burner surface.

Figure 6 Comparison of the mechanisms predictions (U.Lille; KAUST and POLIMI) and measurements (black) at the peak mole fraction in the flame front (top row) and at 8 mm (bottom row) for acetylene, propyne and 1-butyne. Note that linear and logarithmic scales are used.

Figure 7 Comparison of the mechanisms predictions (U.Lille[38]; KAUST and POLIMI) and measurements at the peak mole fraction in the flame front and at 8 mm for benzene, naphthalene and pyrene.

Figure 8 Flame1.60 (top), Flame1.75 (middle) and Flame1.95 (bottom): measured and modeled SVF profiles, using U.Lille (pink), KAUST (green) and POLIMI(blue) mechanisms.

Figure 9: Flame1.75 (top) and Flame1.95 (bottom): measured (symbols) and modeled (lines) pyrene profiles. The dashed and continuous lines represent the predictions obtained respectively without and with coupling of the soot model to the gas phase mechanism.

Figure 10: Primary particle diameters (symbols) measured 1nm-SMPS in Flame1.75 and by HIM in Flame1.95 and modeled particle sphere equivalent diameters distributions using U.Lille (solid lines) and KAUST (dashed lines) mechanisms. The colors represent the different HAB with 3.5mm HAB (red), 6mm HAB (green) and 10mm HAB (blue).

Figure 11: Flame1.75 (top) and Flame1.95 (bottom) soot mass fraction source terms profiles from simulation using KAUST mechanism. Showing nucleation (black) multiplied by 10 (top) and 100 (bottom ULille) and 25 (bottom KAUST), surface growth (red), oxidation (blue) and condensation (green) with its forward (dashed lines) and backward (mixed lines) components

Figure 12: Flame1.95: measured (symbols) and modeled SVF profiles, including modeling without (dashed lines) and with (solid lines) condensation reversibility for U.Lille (pink) and KAUST (green) mechanisms using only pyrene as precursor and KAUST using all PAH larger than pyrene as precursors (blue). The value of α was adjusted in each case to fit the value of SVF in the burnt gases.

Figure 13: Flame1.95: measured (symbols) and modeled pyrene profiles, including modeling without soot model (dashed lines) and with soot model including cases without (mixed lines) and with (solid lines) condensation reversibility for U.Lille (pink) and KAUST (green) mechanisms using only pyrene as precursor and KAUST using all PAH larger than pyrene as precursors (blue).

Figure 14: Flame1.95 modeled particle size distributions at several HAB with (solid lines) and without (dashed lines) condensation reversibility for U.Lille (top) and KAUST (bottom) mechanisms